HARVARD/MIT CENTER
FOR ULTRACOLD ATOMS

PHYSICS DEPARTMENT

MAX-PLANCK-INSTITUTE
FOR QUANTUM OPTICS

Diploma Thesis

A Novel Apparatus for Experiments with Ultracold Fermions

Florian G. Huber

November 17, 2009

Advisers Prof. Markus Greiner
(Harvard University, Cambridge)
and Prof. Gerhard Rempe
(Max-Planck-Institute for Quantum Optics, Garching)

Ultracold neutral atoms in optical lattices are a perfect toy model to simulate and study new physics that appears in the context of high temperature superconductivity. In this work I present the design and construction of a novel apparatus to study these exciting condensed matter systems. Besides this I also investigate a new proposed magneto-optical transport scheme to transport a quantum-degenerate Fermi gas of ultracold lithium atoms into a science chamber.

Contents

1. Introduction

1.1. Quantum Simulation

Understanding how the matter that surrounds us is composed and why it has certain properties has always been of great interest. But it does not necessarily need to be the hunt for the Higgs boson — even on a larger atomic scale, many effects present in solid state systems have not been well understood or are nowadays still not understood although they are more applicable.

Often a simple theoretical model can be proposed, but it cannot be solved due to the huge number of degrees of freedom. Thus in 1947 Bragg and Nye[1] developed the bubble raft, where they used a two dimensional lattice of small bubbles ($< 2\,\text{mm}$ in diameter, up to $100,000$ bubbles) as a toy model. They could experimentally study defects, dislocations, grain boundaries and even apply external forces to compress and shear the lattice. At that time it was neither possible to numerically simulate the many-body problem (computers were just being developed) nor to directly observe defects in a crystal (electron microscopes did not have the required resolution yet).

Today the focus is shifted towards the electronic structure of condensed matter systems, for example the *high-temperature superconductors*, but also other electronic and magnetic

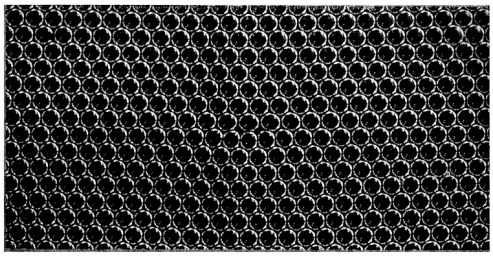

(a) Bragg bubble raft[1]: Condensed matter simulation in 1947...

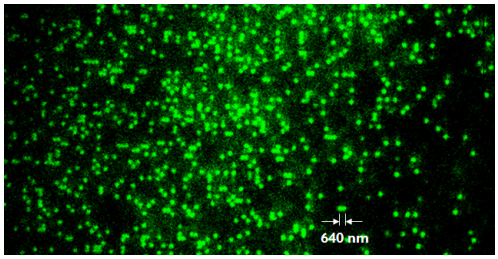

(b) ...and today, the quantum gas microscope[2], 2009

Figure 1.1. Development of condensed matter simulation

materials. Current in a superconductor in general is carried by pairs of electrons (fermions) forming bosonic *Cooper pairs*. In the BCS theory[3] electron-phonon interaction leads to an effective attractive long-ranged interaction between a pair of electrons that intrinsically repell each other due to the Coulomb interaction.

However this theory cannot explain the existence of superconductors with critical temperatures T_c above 30 K. The process leading to high-T_c superconductivity is still one of the unsolved problems in modern physics. In contrast to *s*-wave symmetry for the conventional phonon-mediated superconductors it is believed that the pairing-wavefunction has *d*-wave symmetry[4] in high-T_c superconductors like the "famous" yttrium barium copper oxide YBCO. The pairing there is supposed to happen because of electron-electron interaction.

Following Bragg's approach of building a toy model and combining it with Feynman's idea to simulate a quantum system by using another quantum system[5], the field of *quantum simulation* uses atomic physics methods to model and investigate many-body condensed matter systems. Ultracold atoms[6] with temperatures on the nanokelvin scale which represent the electrons, are embedded into one, two or three-dimensional optical lattices. Atomic, molecular and optical physics provides countless different tools to manipulate and observe the model electrons thus making ultracold atoms the ideal choice to study new physics.

We are building a novel apparatus for experiments with ultracold fermions with exceptional optical access in a dedicated science chamber. Besides trying to simulate and study the high-T_c superconductivity described in detail below, our apparatus also enables us to study new in-lattice cooling mechanism[7] or to perform single-site resolution with the quantum gas microscope demonstrated by [2].

1.2. *d*-Wave Superfluidity in a Hubbard Model and in Plaquettes

The simplest theoretical model that is supposed to be able to describe high-T_c superconductivity (amongst other effects) is the *Fermi-Hubbard model* (see figure 1.2), governed by the *Fermi-Hubbard Hamiltonian*[8]

$$\hat{H} = -J \sum_{\langle i,j\rangle,\sigma} \left(\hat{c}^\dagger_{i,\sigma} \hat{c}_{j,\sigma} + \hat{c}^\dagger_{j,\sigma} \hat{c}_{i,\sigma} \right) + U \sum_i \hat{n}_{i,\uparrow} \hat{n}_{i,\downarrow} + \sum_{i,\sigma} \epsilon_i \hat{n}_{i,\sigma}. \tag{1.1}$$

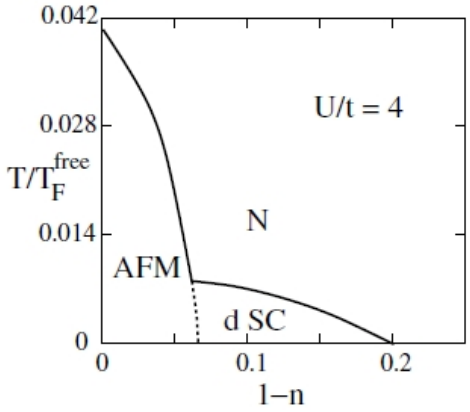

Figure 1.2. Predicted phase-diagram for the Fermi-Hubbard model. It exhibits, depending on the spin imbalance, both anti-ferromagnetic Néel order and the d-wave superfluid, believed to be the mechanism of high-T_c superconductivity.

This model describes fermionic particles in two spin states $\sigma \in \{|\uparrow\rangle, |\downarrow\rangle\}$ in the lowest band of a periodic lattice potential. The atoms can tunnel between the sites with a tunnel matrix element J. A higher J leads to more delocalized atoms and thus can lower the energy of the system due to the Heisenberg uncertainty principle: $\Delta x \Delta p \geq \hbar/2$. In addition there is the on-site interaction energy U for two atoms with opposite spins on the same lattice site. Any external confinement typically present in the experiments described in the following is accounted by the energies ϵ_i. The operators $\hat{c}^\dagger_{i,\sigma}$ and $\hat{c}_{i,\sigma}$ in 1.1 are fermionic creation and annihilation operators, $\hat{n}_{i,\sigma} = \hat{c}^\dagger_{i,\sigma}\hat{c}_{i,\sigma}$ the operator counting the number of fermions on a lattice site i.

Up to now this model cannot be solved in general and for example it is still unclear if its ground state really can exhibit d-wave superfluidity. Neutral atoms in an optical lattice have proven to be ideal to simulate such a Hamiltonian. For example the Mott insulator phase, where all atoms are localized on the lattice sites, has been achieved in this systems[9, 10, 11].

Complete control over the parameters of the Hamiltonian (1.1) is possible: the tunneling J can be controlled by tuning the depth of the lattice, the on-site interaction U by magnetic Feshbach resonances[12] (scattering resonances with one atomic and one molecular channel) and the external confinement energies ϵ_i by changing the focusing of the lattice laser light. The initial properties (filling factor, temperature) of the atoms in the lattice are controlled by the way they are prepared prior to loading them into the lattice.

Instead of cooling a imbalanced spin-mixture in Fermi-gas far below the degeneracy temperature T_F, then ramping up the lattice and hoping for the best, we pursue a different

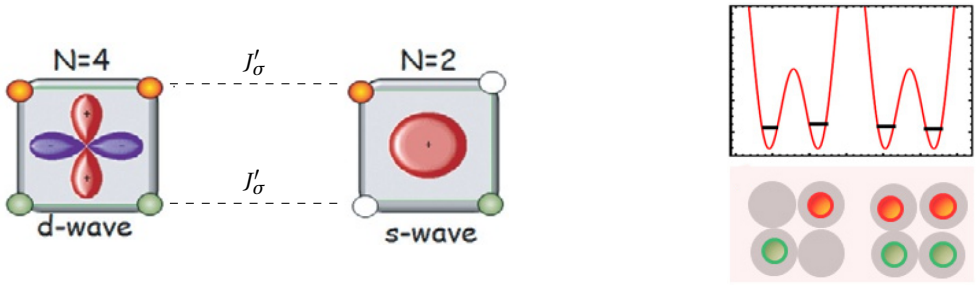

Figure 1.3. Depending on the filling factor, the plaquettes created can exhibit both s-wave and d-wave symmetry.

plan to investigate d-wave superconductivity in ultracold atoms in a bottom-up approach. With the scheme proposed by [13] it is possible to start with small, well-understood systems similar to double wells demonstrated in [14].

In this case the small system, called plaquette, is a 2×2 isolated mini-lattice. The intra-plaquette tunneling is denoted by J and the interaction by U. It can be shown that the ground state for *two* repulsive fermions (on four available sites) $|2\rangle$ in the plaquette shows *s-wave symmetry* while for *four* fermions $|4\rangle$ it exhibits *d-wave symmetry* (figure 1.3). If one now couples two plaquettes with a weak, positive inter-plaquette tunneling J' it turns out that states with three fermions on a single plaquette $|3_i\rangle$ can be energetically suppressed as long as the tunneling is smaller as the binding energy of a hole-pair on a single plaquette.

$$0 < J' < \Delta_b = 2E_0(N=3) - E_0(N=4) - E_0(N=2)$$

Thus the atoms preferably tunnel pairwise between the states $|4,2\rangle$ and $|2,4\rangle$. States with three atoms per plaquette can only be virtual intermediate states mediating a superexchange interaction.

By treating the states with four $|4\rangle \equiv \Uparrow$ and two atoms $|2\rangle \equiv \Downarrow$ per plaquette as pseudo spins, adding a spin-dependency to the inter-plaquette tunneling $J' \rightarrow J'_\sigma$ and extending the plaquette to two-dimensional lattice the system effectively can be described by a Heisenberg XXZ Hamiltonian

$$H_{\text{eff}} = \sum_{\langle i,j \rangle} \sum_{u=x,y,z} J^u \sigma_i^u \sigma_j^u - \mu_z \sum_i \sigma_i^z,$$

where the coupling $J^x = J^y \equiv J^\perp$, J^z depend on the inter-plaquette tunneling and μ_z denotes the energy necessary for adding a pair of atoms to a plaquette. For $J^z/J^\perp < 1$ this system can exhibit a d-wave superconducting phase - exactly what we want to study.

1.3. Next Generation Fermi-Hubbard Quantum Simulator

In this thesis I am going to present the design and construction of a new apparatus that will serve as a next generation quantum simulator. It will enable us to study Fermi-Hubbard physics with neutral atoms in optical lattices.

We have chosen Lithium $^6_3$Li for our experiment. This species has a broad Feshbach resonance at an easily achievable magnetic field strength of around 830 G[15] making controlling of interaction between the atoms feasible, an important ingredient for the study of the Fermi-Hubbard model. Another fact, both advantage and disadvantage, is its light mass of only 6 amu, which leads to a large recoil energy

$$E_{\mathrm{rec}} = \frac{\hbar k_{\mathrm{L}}}{m}.$$

On one hand this increases the tunneling rate in a lattice and thus reduces the time constant for dynamic processes in the lattice compared to heavier species. But on the other hand this also requires high-power lasers to freeze out the tunneling by making the lattice very deep, for example in order to go to the Mott-insulator phase. Thus we are planning to use enhancement cavities (similar to [16]) to increase the effective laser intensity of the optical lattice.

One problem inherent to cooling all fermions is that once temperatures on the order of the Fermi temperature T_{F} are reached evaporative cooling does not work properly anymore. The atoms cannot thermalize because the Pauli exclusion principle forbids *s*-wave scattering between two atoms in the same state, the only scattering process that still would possible for atoms at such ultracold temperatures. To overcome this limitation in our experiment lithium will be sympathetically cooled with bosonic sodium $^{23}_{11}$Na Bose-Einstein condensate. Sodium is evaporated and thermalizes with the lithium cooling it further below T_{F}. This way we can achieve bigger atom numbers than single-species lithium machine that are using a spin-mixture for sympathetic cooling instead.

One of the outstanding features of our apparatus (figure 1.4) will be the large optical access that is granted by a dedicated science chamber. All preparation of the atoms including the magneto-optical trap and further cooling to quantum degeneracy will be shifted to a main chamber, so that the science chamber itself is “clean” meaning that there is no optics that is not going to be used for the actual experiment. This enables us to implement a three-dimensional optical lattice and even put enhancement cavities inside the chamber

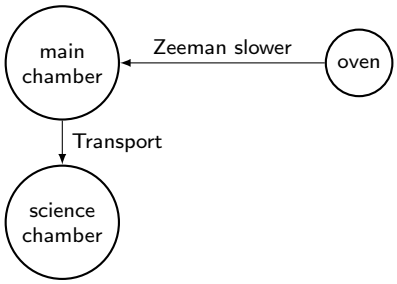

Figure 1.4. Simplified schematic of our apparatus.

to create deep lattices. With this setup we are also able to create the necessary superlattices to study the d-wave superfluidy as described in the previous section.

In order to transport the ultracold quantum gases between the two chambers, we propose a novel magneto-optical transport scheme described in detail in chapter 6. It promises larger atom numbers than existing methods due to a larger trapping volume and better mode matching with other traps.

Together with my co-workers I designed and built this novel apparatus during the last year. In the time of my diploma thesis we managed to achieve trapped sodium atoms in a magneto-optical trap. In addition to that I investigated the heating that could be caused by magnetic field disturbances in the magneto-optical transport in detail.

1.4. Structure of this work

This work is structured as follows:

- The next chapter gives an introduction into the light-matter interaction that is required to understand the principles of the Zeeman slower and the magneto-optical trap and mostly follows [17].
- In the third chapter the path of the atoms from the source into the main chamber is sketched together with a detailed description of the machine. Wherever necessary additional theory will be introduced.
- The forth chapter deals with magneto-optical trap, the related loss mechanisms and ways to avoid them.
- Chapter five very briefly describes the missing parts to get a sodium Bose-Einstein condensate and a degenerate Fermi gas of lithium atoms.

- The sixth chapter explains a novel magneto-optical transport scheme for degenerate quantum gases and shows how we studied the technical feasibility of this approach.
- In the seventh chapter a method to control the beam pointing of our dye laser is presented.
- The last chapter concludes this work and gives a brief outlook of the next milestones of the experiment.

2. Light-Matter-Interaction

2.1. Motivation

The following sections provide a brief overview of the theoretical foundations of light-matter interaction. This is required to understand Zeeman slowing and the magneto-optical trapping in the next chapters.

2.2. Density Matrix Formalism

The quantum mechanical treatment of a quantum system that is coupled to the environment is different formalism than the Schrödinger equation. The state of the system is described using the *density matrix*

$$\hat{\rho} = \sum_i p_i \left|\Psi_i\right\rangle \left\langle\Psi_i\right|,$$

where $|\Psi_i\rangle$ denotes a *pure state* of the ensemble and p_i the probability to find the system is this state.

The density matrix formalism expectation value of an observable $\hat{O}$ of the system is given by:

$$\left\langle \hat{O} \right\rangle = \sum_i p_i \left\langle\Psi_i\right| \hat{O} \left|\Psi_i\right\rangle = \mathrm{tr}\left(\hat{\rho}\hat{O}\right)$$

In general the time evolution of the density matrix is simply given by the von-Neumann equation

$$i\hbar \frac{\partial}{\partial t}\hat{\rho} = \left[\hat{H}, \hat{\rho}\right] \tag{2.1}$$

For example the density matrix of a two-level atoms with ground state $\left|\mathrm{g}\right\rangle$ and excited state $|\mathrm{e}\rangle$ is represented by a 2×2 hermitian matrix

$$\hat{\rho} = \begin{pmatrix} \rho_{\mathrm{ee}} & \rho_{\mathrm{eg}} \\ \rho_{\mathrm{ge}} & \rho_{\mathrm{gg}} \end{pmatrix}. \tag{2.2}$$

The diagonal elements are the probabilities to find the atom in these states and the off-diagonal elements ($\rho_{eg} = \rho_{ge}^*$) are the coherences between the two states.

2.3. Optical Bloch Equations

Applying this formalism to the atom-field-interaction with a simplified Hamiltonian

$$\hat{H} = \hat{H}_A + \hat{H}_L + \hat{V}_{AL}^c$$

explains several important effects necessary to understand laser cooling. $\hat{H}_A$ is the Hamiltonian for a two-level atom at rest with the ground and excited state $|g\rangle$ and $|e\rangle$ with the energy difference $\hbar\omega_0$:

$$\hat{H}_A = \hbar\omega_0 |e\rangle \langle e| .$$

The light field Hamiltonian $\hat{H}_L$ can be neglected in this context as we assume that we are not in the single-photon regime, i.e. taking one photon out of the light field approximately does not change the total number of photons. The semiclassical light-matter interaction Hamiltonian in dipole and rotating wave approximation $\hat{V}_{AL}^c$ is given by

$$\hat{V}_{AL}^c = -e\mathbf{E}(\mathbf{r}, t) \cdot \hat{\mathbf{r}},$$

where the electric field of the laser is given by $E(\mathbf{r}, t) = E_0 e^{i(\mathbf{k}\cdot\mathbf{r} - \omega t)}$ and the operator $\hat{\mathbf{r}}$ defines the *Rabi frequency* by its matrix element

$$\Omega \equiv -\frac{e}{\hbar} E_0 \langle e| \hat{\mathbf{r}} |g\rangle .$$

This gives rise to following differential equations describing the time evolution of the two-level density matrix:

$$\begin{aligned}
\dot{\rho}_{gg} &= -\frac{i}{2}\left(\Omega\rho_{ge} - \Omega^*\rho_{eg}\right) \\
\dot{\rho}_{ee} &= \frac{i}{2}\left(\Omega\rho_{ge} - \Omega^*\rho_{eg}\right) \\
\dot{\rho}_{ge} &= i\delta\rho_{ge} + i\frac{\Omega^*}{2}\left(\rho_{ee} - \rho_{gg}\right) \\
\dot{\rho}_{eg} &= -i\delta\rho_{eg} + i\frac{\Omega}{2}\left(\rho_{ee} - \rho_{gg}\right)
\end{aligned}$$

If one now also takes the spontaneous emission with the excited state lifetime $1/\gamma$ as the

only relaxation process (no dephasing due to scattering in the ensemble, etc.) into account, this equations lead to the *optical Bloch equations*:

$$\begin{aligned}
\dot{\rho}_{gg} &= \gamma\rho_{ee} - \frac{i}{2}\left(\Omega\rho_{ge} - \Omega^*\rho_{eg}\right) \\
\dot{\rho}_{ee} &= -\gamma\rho_{ee} + \frac{i}{2}\left(\Omega\rho_{ge} - \Omega^*\rho_{eg}\right) \\
\dot{\rho}_{ge} &= -\left(\frac{\gamma}{2} + i\delta\right)\rho_{ge} + i\frac{\Omega^*}{2}\left(\rho_{ee} - \rho_{gg}\right) \\
\dot{\rho}_{eg} &= -\left(\frac{\gamma}{2} - i\delta\right)\rho_{eg} + i\frac{\Omega}{2}\left(\rho_{ee} - \rho_{gg}\right)
\end{aligned}$$

The steady state solution for the excited state population shows *power broadening*. Its dependence on the detuning $\delta = \omega_L - \omega_0$ of the laser light is

$$\rho_{ee} = \frac{s_0/2}{1 + s_0 + (2\delta/\gamma)^2}, \tag{2.3}$$

where the *saturation parameter* s_0 is defined as

$$s_0 \equiv 2\left|\Omega\right|^2/\gamma^2. \tag{2.4}$$

This in turn also defines the *saturation intensity* I_s by $s_0 = I/I_s$, which also depends on the atom species. One can see that even for infinite laser power $s_0 \to \infty$ the maximum excited state population is 50 %.

2.4. Radiation Force

An atom described by the optical Bloch equations can absorb photons with the scattering rate

$$\gamma_s = \gamma\rho_{ee}.$$

Every time it absorbs a photon it gets kicked with the photon momentum $\hbar k_L$. This momentum transfer leads to the radiation force

$$F_{rad} = \hbar k_L \gamma \rho_{ee}. \tag{2.5}$$

The spontaneous emission afterwards does not lead to a momentum transfer on average, because the emission has uniform probability distribution over the whole 4π solid angle.

Despite this force there is another light force that depends on the intensity gradient instead of the absolute intensity, the so called *dipole force*. This force is exploited in optical dipole traps or optical lattices, but it is not important for the understanding of the Doppler cooling mechanisms.

3. From the Source to the Main Chamber

3.1. Motivation

This chapter describes to path of the not-yet-ultracold atoms from the oven source through the Zeeman slower, where the already get slowed down to velocities equivalent to a few Kelvin, into the main chamber. In addition an overview over our whole vacuum setup is given together with our experiences during the back-out.

3.2. Vacuum Setup

3.2.1. Overview

One challenge that all Bose-Einstein condensate experiments have in common is that the fragile BEC phase requires extreme conditions. The phase transition happens when the thermal deBroglie wavelength

$$\lambda_T = \sqrt{\frac{2\pi\hbar^2}{m k_\mathrm{B} T}}$$

of an ensemble of bosonic atoms with mass m and temperature T becomes comparable with the interparticle spacing $n^{-1/3}$, where n denotes the density in the ensemble. For typical densities achieved in an experiment the critical temperature T_C is on the order of 100 nK[18]. Besides having "unconventional" cooling mechanisms described in section 4.2, to be able to achieve this temperatures the atoms also have to be very well isolated from the environment. This requires the vacuum chamber to have an extremely low pressure on the order of 10^{-11} Torr in the ultra-high vacuum (UHV) regime, because collisions with the background gas are the main source for external heating[1]. In addition to using effective

[1] Thermal radiation can be neglected for cold atoms, because there is only little energy in the thermal spectrum within the narrow absorption lines of the atoms.

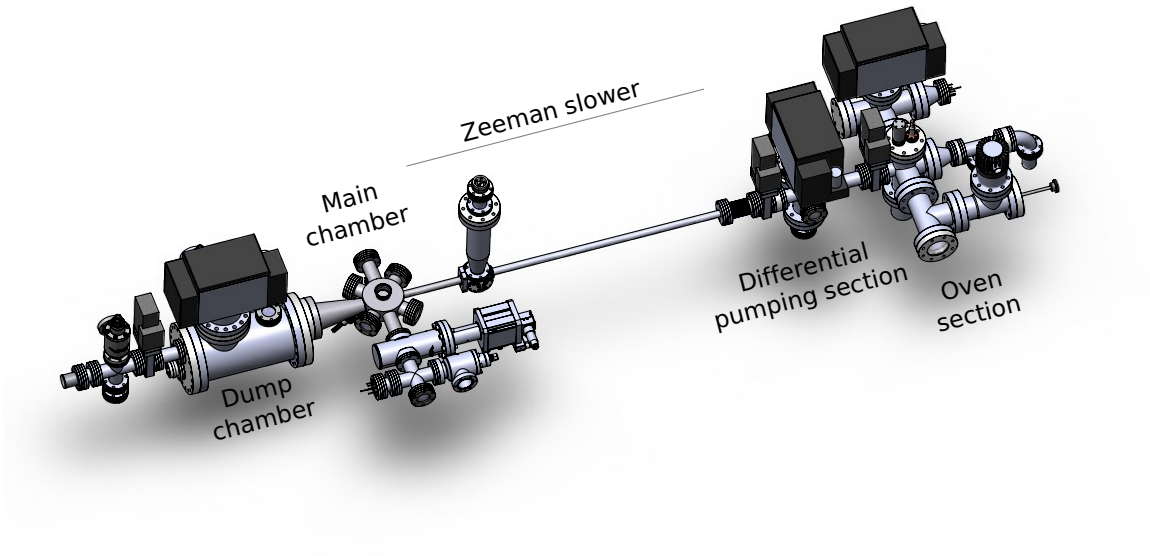

Figure 3.1. Three-dimensional model of the vacuum chamber.

pumps suited for such pressure, the chamber has to be baked to reduce the outgassing from the metal parts (see section 3.2.2).

The whole system is roughly 2.75 m long (figure 3.1). The atoms start on the right side in the two-species sodium/lithium oven (section 3.3) at a temperature of 450 °C and a pressure of about 10^{-3} Torr[19]. This equals velocities of 700 m/s for sodium and 1400 m/s for lithium with densities of around 10^{10} 1/mm³ compared to 10^{16} 1/mm³ at atmosphere. After the nozzle inside the oven chamber the background pressure is at $5 \cdot 10^{-8}$ Torr with densities of 10^{6} 1/mm³. To isolate this section from the actual UHV in the main chamber it is followed by a differential pumping tube (0.18 in ID, 5.65 in long) and another intermediate chamber ("differential pumping chamber") with another ion pump. We already achieve a pressure below 10^{-9} Torr there. This section in turn is separated with another differential pumping tube (0.18 in ID, 3.36 in long) from the Zeeman slower (see section 3.4), where the atoms inside the atomic beam are slowed down by more than one order of magnitude.

The slow atoms are then loaded into a magneto-optical trap inside the main chamber, where additional cooling is performed (see chapters 4 and 5). The atoms that are not captured from the atomic beam hit the heated Zeeman slower window on the very end of the chamber, before they eventually get pumped away inside the dump chamber. In addition

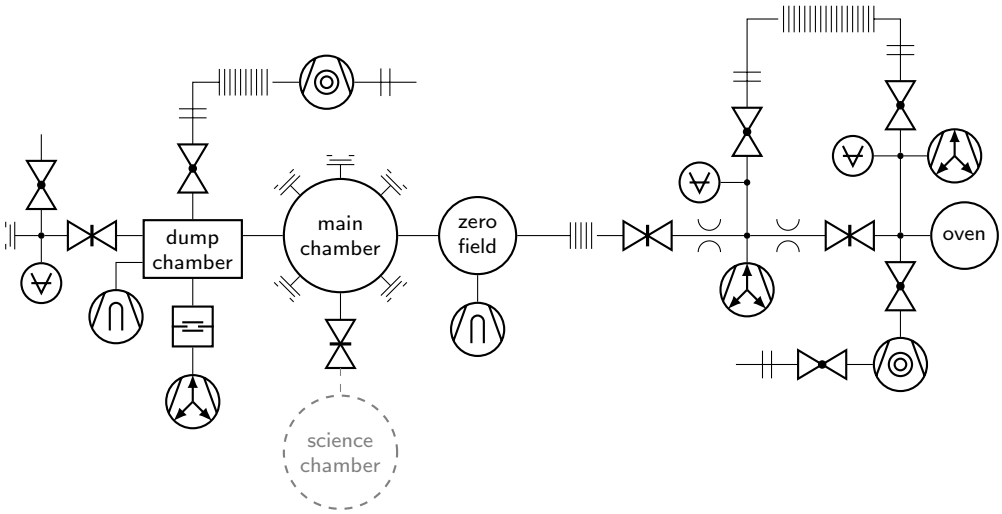

Figure 3.2. Schematic representation of our vacuum system. The forevacuum is omitted.

to the ion pump there, the main pumping is done by a Titanium sublimation pump that uses the whole dump chamber surface area to pump. This provides us a pressure of the order of 10^{-11} Torr, which is equivalent to a density of only 300 atoms of background gas per $1\,\mathrm{mm}^3$.

The main sections of our vacuum system are all separated by gate valves to be able to vent the sections independently. This for example is necessary when the alkali atoms in the oven are used up and has to be replaced. A detailed schematic of the apparatus is given in figure 3.2. The gate valve separating the yet to be designed science chamber from the main chamber is a non-magnetic all-metal gate valve from VAT. All the other gate valves are Viton sealed gate valves with pneumatic actuators from LESKER.

3.2.2. Baking

3.2.2.1. Temperatures

In order to achieve the desired vacuum pressures in the UHV regime of around 10^{-11} Torr it is crucial that the vacuum chamber is heated to temperatures of about 200 °C for an extended period of time. The higher temperatures exponentially speed up the outgassing of gasses that had been absorbed by the stainless steel under atmosphere (e.g. Hydrogen, Nitrogen) or that are coating the stainless steel (like water). This is due to the temperature dependence of the diffusion constant[20]. From our baking curves one can defer an improvement of one order of magnitude in the final pressure with roughly every 40 °C increase

in temperature (see section 3.2.2.4 and especially figure 3.5)

At even higher temperatures (400 °C) it would even be possible to decompose possible hydrocarbon oils that could have remained on some parts from the machining process when not properly cleaned.

However the some of the vacuum components restrict the maximum possible temperature. The vacuum tubes and the CF flanges are usually rated to 400 °C and higher and thus are not a problem, except that one should use nickel or silver plated copper gaskets to prevent the gasket fusing to the flange. Also electrical feedthroughs with ceramic insulation could be baked at this temperature.

In our case the temperature was limited by the non-magnetic viewports on the main chamber. The lead alloy used to seal the glass to the flange can only sustain 200 °C. After one viewport started to leak in the early baking process (probably due to local overheating), we decided to limit the temperature on all viewports to 180 °C.

In addition to that the Viton sealed gate valves that are used in three places in the machine are also rated to 200 °C, but a KURT J. LESKER engineer strongly recommended baking below 150 °C even in the opened position. Other sources[21, 22] indicate that it is possible to bake Viton up to 290 °C for a limited time before the plastic starts decomposes. Trying to maintain temperatures at around 160 °C to 170 °C seemed to be a good compromise for us.

It also does not make sense to have other areas significantly hotter, because otherwise vapor could condense again on the colder spots and is not pumped away. Having this in mind we tried to achieve a temperature of 180 °C everywhere. The actual achieved temperatures are given in table 3.1 and the zones correspond to figure 3.3.

3.2.2.2. Zones

Controlling the temperatures was achieved using TEMPCO TEC9300 PID temperature controllers that were doing pulse width modulation on OMEGA silicone insulated heater tapes (maximum temperature 260 °C) by driving a CRYDOM D2425 solid state relay. For the feedback a K-type thermocouple was attached between two windings of the heater tape on top of the first aluminum foil layer using high temperature Kapton tape with silicone adhesive backing (MCMASTER 7648A34).

The whole chamber was divided into 17 (+1 spare) such zones that each had separate feedback. In order to monitor the temperatures we added 70(!) additional K-type thermocouples, especially one for each viewport. Their temperatures were measured using five OMEGA CN612 controllers, which also where used as emergency interlock and would have

Table 3.1. Temperatures achieved during the initial bake-out of our vacuum chamber in the various zones.

#	Description	Wattage (W)	Average Temp (°C)
1	Zeeman slower window	313	160
2	Dump chamber	630	170
3	Dump chamber elbows	261	175
4	Main chamber	313	170
5	Transport	313	170
6	Zero field chamber	156	195
7	TiSub	209	190
8	Zeeman slower decreasing	104	195
9	Zeeman slower start	208	170
10	Differential chamber	313	165
11	Oven (around cold plate)	417	160
12	Oven (under ion pump)	313	175
13	Oven (“Turbo T”)	206	155
14	Bypass	313	195
15	Dump chamber ion pump	313	180
16	Differential chamber ion pump	313	185
17	Oven chamber ion pump	261	180

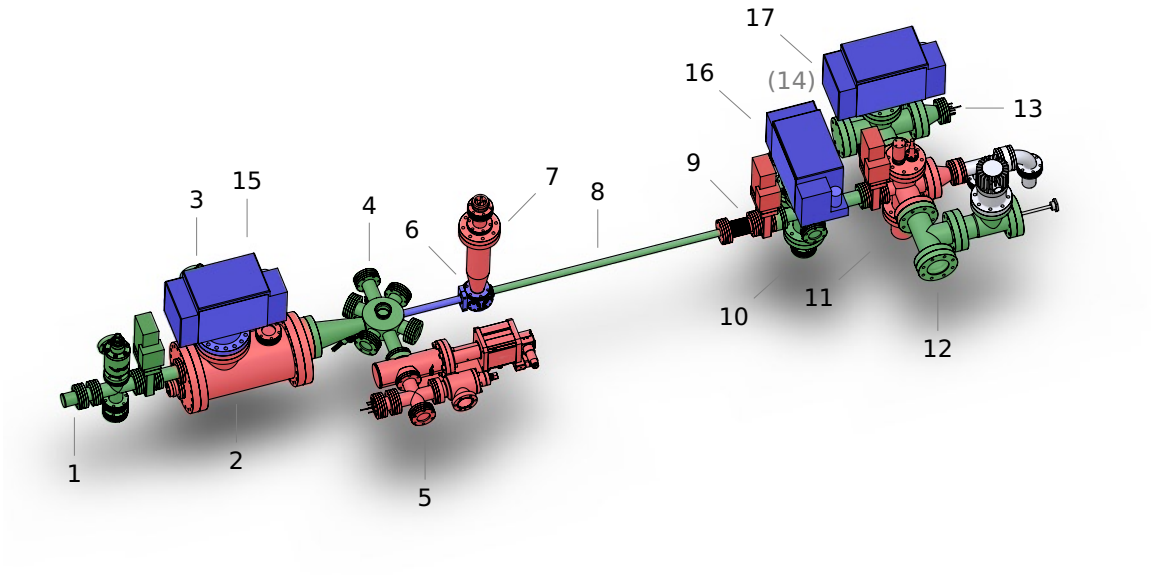

Figure 3.3. Different temperature zones during the bake-out. Each of these zones has its own temperature controller. The numbers correspond to table 3.1.

should down all heaters in case a temperature limit was exceeded[2]. All temperatures have been logged to the computer.

The reason why we had such a large number of thermocouples is that we found that there were some fairly large temperature gradients (up to 25 °C) even within one zone. This in turn could cause local overheating of some components. We believe that this effect caused by a leaking viewport due to a partially molten seal in an earlier baking-out attempt.

With the finer grained temperature monitoring, we also could reduce the gradients by adding or removing more insulation and adding some smaller variac controlled constant power heater tapes. However this is not trivial. Adding more insulation close to the feedback thermocouple, for example, will actually reduce the temperature elsewhere in the zone. Only small adjustments should be made in order to keep the system close to equilibrium.

Each of the three ion pumps was a separate zone. The new design of the decreasing section of the Zeeman Slower allowed us to directly heat the vacuum tube from the inside

[2] Note that there is a ≈ 5 s delay in those controllers before the interlock trips. This makes them useless for time critical interlock applications where fast heating rates are expected such as monitoring the temperature of the quadrupole coils.

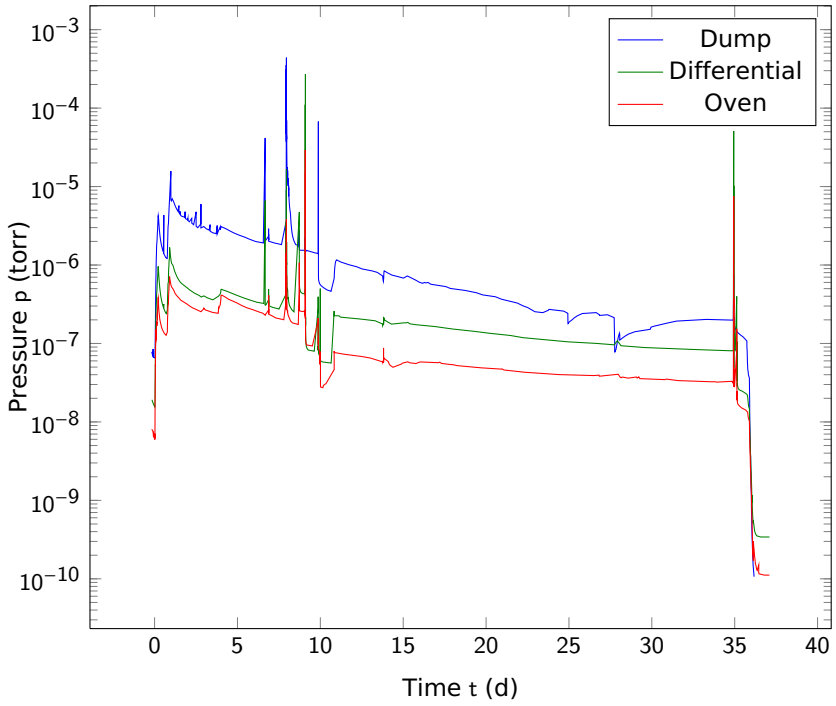

Figure 3.4. Pressures during the bake-out in different sections of the vacuum chamber.

of the tube on which the coil is wound. The remaining zones where distributed over the chamber as depicted in figure 3.3.

3.2.2.3. Wrapping the chamber

In order to heat the chamber to the desired temperature the chamber has to be wrapped with the heater tapes and then insulated. We first added a single layer of aluminum foil that tightly wraps the vacuum parts. The reason was to have a more uniform heating and suppress possible temperature gradients. To protect the viewports from scratching Kapton tape was attached to the foil in those areas.

After adding the heater tapes an additional tight layer of aluminum foil is attached, before adding multiple layers of crumpled aluminum foil as thermal insulation. We found that it is important that the insulation layers do not leave big air pockets. The convection inside would heat the parts on the top significantly hotter than those on the bottom.

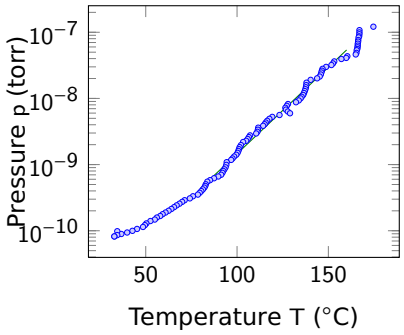

Figure 3.5. Temperature dependence of the pressure in the main chamber during the cool down.

3.2.2.4. Actual Baking

The temperature was ramped up with roughly 20 °C/h in two steps to the final temperature. Those temperatures given in table 3.1 were kept through the whole 36 days of baking. The initial pressures were already between 10^{-7} Torr and 10^{-8} Torr due to a previously failed baking attempt (leaking viewport).

After one week of baking the VARIAN titanium sublimation pumps where continuously degassed at 32.5 A according to the specs. The pressure almost spiked up to 10^{-3} Torr, when we started to run current through them. It is important to degas the titanium rods during the bake-out, because they contain a lot of contamination. But we suspect that this current was too high and that we actually fired the pumps the whole time. Having this suspicion the degassing was ended on day 27. Until now it is not obvious if we used up all the titanium during the degassing procedure.

Because the ion pumps were wrapped with the magnets assembled, we also turned them on for a couple of days in the second week of the baking in order to degas. The ion pumps are not supposed to saturate at this high temperature, even though the pressure is pretty high.

Before the final cool down the ion pumps have been turned on again. The turbo molecular pumps stayed on almost until the very end of the cool down. We experienced that they only start to have some backflow below 10^{-10} Torr.

From the change of the pressures during the cool down (figure 3.5), one can deduct that once the temperature dependence of the pressure in the steady state (outgassing rate = pumping) is described by an exponential function. The pressure improves by one order of magnitude by cooling down the system by 40 °C.

3.2.2.5. Leak checking

Searching for small leaks is done by connecting the leak checker (LEYBOLD PhoenixXL 300) to the forevacuum side of the turbo molecular pumps. It has a mass spectrometer built in that can detect helium-4. If one sprays some helium onto a leak the helium-4 rate detected in the leak checker immediately increases.

It is important to know that the rubber O-rings used in QuickFlange/KF connections have high helium permeability. Buna-N rings are slightly better in this respect than Viton gaskets. In any case this limited the time we could do leak checking on a reasonably low background to roughly ten minutes, because the leak checker was connected via several KF-flanged bellows to the chamber. After that it took roughly six to twelve hours to recover the saturated gaskets at room temperature.

For larger leaks one can also drop methanol or acetone onto the suspected leaking parts. The methanol/acetone vapor inside the chamber changes the reading of the ion gauge. In our case the pressure increased by a factor of 4 with methanol when there was a leak. The problem with this method is that the liquid can actually seal the leak for a couple of hours (especially smaller leaks). In this case no more helium leak checking is possible. A quick re-bake this area helped in our case to open the leak again.

3.3. Two-Species Atomic Beam Oven

In comparison to most BEC experiments working with Rubidium, it is not feasible to capture sodium and lithium from the background gas at room temperature, because the vapor pressure of the lighter alkali elements is lower. Thus it is required to heat those to higher temperatures inside an oven.

We are using an oven design based on [19]. In order to prevent one species diffusing into the other species oven, it is crucial that the temperatures of the different sections of the oven (figure 3.8) are correct. Besides loosing atoms from the atomic beam, this could change the vapor pressure compared to a “pure” reservoir and stopping the oven from working properly. In addition the backflow of lithium into the sodium reservoir is suppressed by the particular design of the nozzle such that the lithium gets pushed out of the nozzle by the sodium. In our setup the temperature of the reservoirs is 360 °C for sodium and 380 °C for lithium. The two species are then mixed in the mixing chamber at 450 °C. This high temperature prevents them from forming an alloy, but also requires taking additional precautions such as using 316 stainless steel flanges and nickel gaskets.

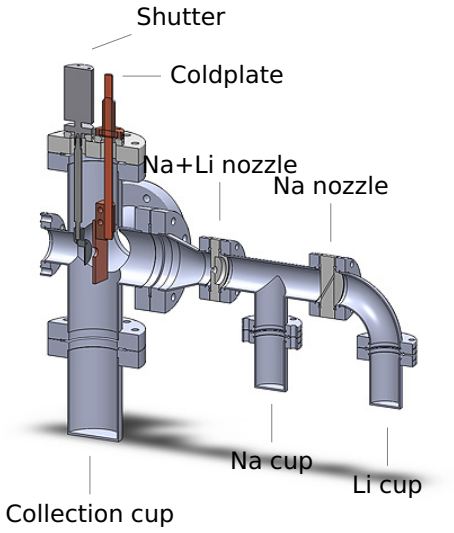

Figure 3.6. Three dimensional model of the oven assembly.

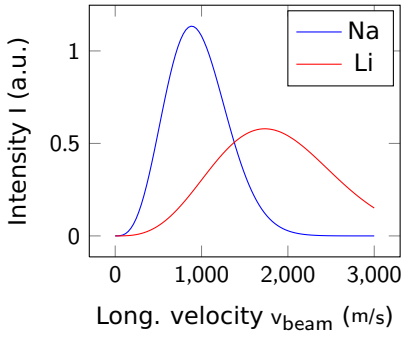

Figure 3.7. Theoretical initial velocity distribution in the atomic beam in the longitudinal direction for a source temperature of 450 °C.

The generated sodium/lithium two component atomic beam has a temperature of 450 °C. The coldplate collimates the beam and therefore cuts the transverse velocity distribution in the beam, i.e. all atoms already have low velocity in that direction. In the longitudinal direction the initial velocity is about 890 m/s for sodium and 1700 m/s for lithium respectively (figure 3.7). Note that these velocities differ by a factor of $\sqrt{3/2}$ from the most probable velocities from a Maxwell-Boltzmann distribution, because the aperture only selects a particular direction and thus gives rise to a different velocity distribution in the atomic beam[23].

In addition to the collimation the coldplate can also act as a pump if it is cooled. The peltier cooling is going to be added in the next upgrade of our experiment. In our design the coldplate is made out of 0.125 in thick copper with a 0.4 in bore. It is connected to a high-power copper feedthrough as depicted in figure 3.8. The plan is to heat the coldplate from the air side in order to melt away all the accumulated sodium and lithium, before it can clog the bore. Before it was put under vacuum the copper plate and the adapter had been etched in 30 % hydrochloric acid. This step removed the porous oxide layer from the copper.

Following the coldplate there is the atomic beam shutter constructed from a magnetic rotary feedthrough that rotates the shutter out of the beam. It is actuated by an external

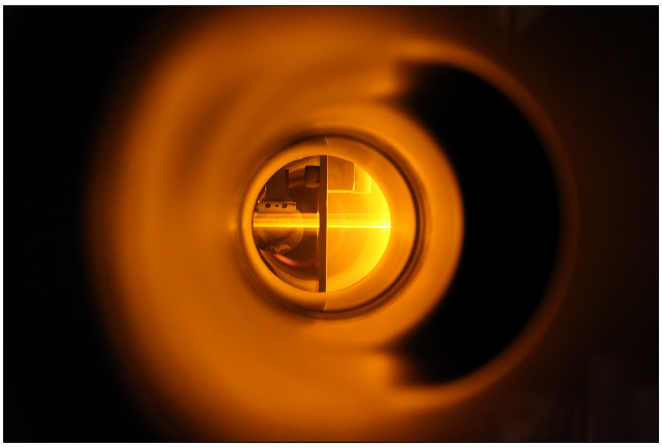

Figure 3.8. A strong flourescence from the sodium atoms on the oven side (right) of the coldplate (center) can be seen. There is also flourescence in the colimated atomic beam (left) that is passing the opended shutter.

servo motor to have reproducible fast actuation times. The function of the shutter is to unblock the atomic beam to load the MOT in the main chamber and to block it after that. A continuous flux of atoms would cause heating during the evaporation step and prevent the BEC from being formed.

The atomic beam oven with coldplate and shutter can be seen in operation in figure 3.8.

3.4. Spin-Flip Zeeman Slower

3.4.1. Theory

3.4.1.1. Magnetic Field Profile

As mentioned in section 3.3 the atoms exiting the oven have high velocities in the longitudinal direction (positive z direction) and the vast majority of them are far to0 fast to be captured in a magneto-optical trap. The idea of a Zeeman slower[24] is to use a laser beam propagating in the opposite direction to slow down the atoms by scattering photons.

On one hand each photon that is absorbed by an two-level atom transfers an momentum of $\mathbf{p}_\mathrm{L} = \hbar\mathbf{k}_\mathrm{L}$ ($\approx 0.03\,\mathrm{m/s}\cdot 23\,\mathrm{amu}$ for sodium, $\approx 0.1\,\mathrm{m/s}\cdot 6\,\mathrm{amu}$ for lithium) in the opposite direction of the atom's velocity vector. On the other hand the direction spontaneous emission back to the ground state is uniformly distributed over the whole solid angle of 4π, so that there is a net force acting on the atoms in the atomic beam. The limiting factor for the strength of force is the time it takes for the atom to decay to the ground state before

it can absorb another photon. In the high intensity limit for a (approximately) closed cycling transition at most half of the atoms are in the exited state at any given time due to the competition between absorption, spontaneous and stimulated emission. The expression for the radiation force was already introduced in section 2.4 and is given by

$$\mathbf{F}_{\text{rad}} = \hbar \mathbf{k}_{\text{L}} \gamma \rho_{ee},$$

where ρ_{ee} is the population inversion or the probability for an atom to be in the excited state also defined in section 2.3. Thus the maximum possible deceleration that can be achieved is

$$a_{\max} = \lim_{s_0 \to \infty} \frac{|\mathbf{F}_{\text{rad}}|}{m} = \frac{\hbar k_{\text{L}} \gamma}{2}. \tag{3.1}$$

Because the Doppler-shift $\Delta\omega = -\mathbf{k}_{\text{L}} \cdot \mathbf{v}$ the fast atoms experience on the order of 1 GHz is a lot larger than the natural linewidth of the atomic transition ($\gamma = 2\pi \cdot 9.8\,\text{MHz}$ for sodium, $\gamma = 2\pi \cdot 5.9\,\text{MHz}$ for lithium), after a few hundred scattering events into the excited state the light of the slowed down atom is not resonant with the atomic transition anymore. Due to this velocity dependence of the light force, this force is dissipative (like simple velocity dependent friction in mechanics) and can actually slow down.

To compensate for this a Zeeman slower uses the Zeeman shift of the atomic levels $\Delta E_{\text{Z}}(z) = -\mu \cdot \mathbf{B}(z)/\hbar$ in a spatially varying magnetic field $\mathbf{B}(z)$. The magnetic moment μ here is the different in the magnetic moments of the ground and excited state

$$\mu = (g_e m_e - g_g m_g)\mu_{\text{B}} \tag{3.2}$$

of the closed cycling transition and especially its sign depends on the polarization of the laser light (giving $\Delta m_{\text{F}} = \pm 1$). When the slowed down atom travels further along the beam and experiences a different magnetic field, the laser light is resonant again. This leads to following condition for the atoms to stay resonant for a fixed laser detuning $\delta = \omega_{\text{L}} - \omega_0$ from the atomic transition ω_0:

$$-\frac{1}{\hbar}\mu \cdot \mathbf{B}(z) - \mathbf{k}_{\text{L}} \cdot \mathbf{v}(z) + \delta = 0 \tag{3.3}$$

If one now assumes a constant deceleration $a < a_{\max}$ and a initial velocity v_0, the position dependent velocity can be written as

$$v(z) = \sqrt{v_0^2 - 2az}, \tag{3.4}$$

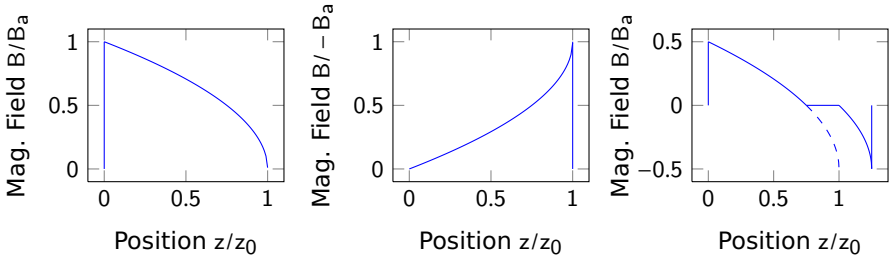

(a) Decreasing field slower. **(b)** Increasing field slower. **(c)** Spin-flip slower with a zero-field section of $0.25 z_0$.

Figure 3.9. Different types of Zeeman slowers.

which in turn makes it possible to solve equation (3.3) for the magnetic field

$$B(z) = \frac{\hbar}{\mu}(\delta + k_{\mathrm{L}} v(z)) = \frac{\hbar\delta}{\mu} + \frac{\hbar k_{\mathrm{L}} v_0}{\mu}\sqrt{1 - \frac{2az}{v_0^2}}. \tag{3.5}$$

We can introduce the length of the Zeeman slower $z_0 = v_0^2/(2a)$ required to completely stop an atom with the initial velocity v_0, the magnetic field at the end $B_0 \equiv B(z_0) = \hbar\delta/\mu$ and the difference of the magnetic fields at the beginning and the end $B_a = \hbar k_{\mathrm{L}} v_0/\mu$. Using this the field profile can be parameterized as follows:

$$B(z) = B_0 + B_{\mathrm{a}}\sqrt{1 - \frac{z}{z_0}} \tag{3.6}$$

It is worth mentioning that even the sign both B_0 and B_{a} can be independently controlled by choosing the sign of detuning δ and μ (dependent on polarization of the laser).

3.4.1.2. Different Types of Slowers

There are mainly three different types of Zeeman slowers. They all have their particular advantages and disadvantages and are all used in different experiments.

Probably the most obvious implementation for a slower is to choose the final field $B_0 = 0$ such that the magnitude of the magnetic field is gradually decreasing (figure 3.9a). The profile gives this slower the name *decreasing field slower*. One problem with this type is that for a zero final velocity the laser beam is tuned to resonance and thus can disturb a magneto optical trap located further downstream. This is of course less severe for a finite final velocity. The small magnetic field at the end also makes it possible to place the slower closer to

a magneto optical trap, because there are less disturbing fields and gradients compared to the following slowers.

The opposite approach would be to choose an increasing magnetic field profile (figure 3.9b) with $B_a = -B_0 \neq 0$. Accordingly this type is called *increasing field slower*. This configuration leads to a farther detuned laser beam, which doesn't perturbate trapped atoms downstream. However the fields at the end are large compared to the decreasing field slower and can again disturb the quadrupole field of a magneto optical trap. This can be circumvented by having a larger distance to the trap at the cost of a reduced flux.

Another design that combines the advantages (and disadvantages) is the so-called *spin-flip Zeeman slower*, which first starts with a decreasing section $|B_0| < |B_a|$where the atoms are already slowed down in a first step (figure 3.9c). At the zero crossing of the slower this section stops and turns into a (ideally) zero field section. The following section is an increasing field slower. As the magnetic field changes sign, i.e. flips direction, the quantization axis changes. Thus the spin of the atoms effectively gets flipped and also the polarization of the slowing beam changes from σ^+ to σ^- or vice-versa. This transition has to be reasonable slow that the atoms can follow, which increases the length of the slower.

There is no "best" Zeeman slower. It is always a tradeoff between flux (length), magnetic field perturbations and final velocities and the optimum slower is different for different experiments and different species. Our system inspired from the MIT design from Wolfgang Ketterle is using also the spin-flip Zeeman slower, because it is used to produce very large sodium MOTs in their system.

3.4.1.3. The Optimum Beam Waist

The radial intensity of a Gaussian beam with a certain total power of P_0 and a waist of w is given by

$$I(r, w) = \frac{2P_0}{\pi w^2} \exp\left(-2\frac{r^2}{w^2}\right).$$

All atoms feeling an intensity of at least $I_{\min} = s_0 I_s$ are slowed down in the Zeeman slower, where I_s is the saturation intensity given in section 2.3. The exact factor s_0 depends on the design of the Zeeman slower and is of the order of $\mathcal{O}(1)$. The radius within the beam where the intensity is equal to the minimum required intensity

$$I(r = r_{\text{cap}}, w) = I_{\min} = s_0 I_s, \tag{3.7}$$

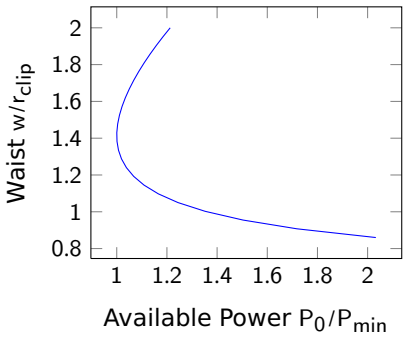

Figure 3.10. Optimum waist w to overfill an aperture with radius r_{clip} for a given power P_0.

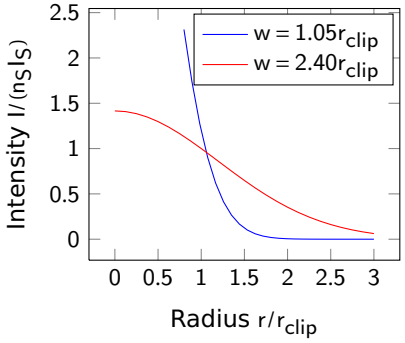

Figure 3.11. Intensity profile of a gaussion beam that fulfills equation (3.7) for $P_0 = 1.5P_{min}$.

defines the capture radius r_{cap} of the Zeeman slower beam. Ideally (for enough power) the waist w is chosen such the radius is identical with radius of any aperture r_{clip} that clips the beam (e.g. the vacuum tube itself, differential pumping tubes, etc.).

$$r_{clip} = r_{cap}$$

If one attempts to solve for the ideal waist, the general solution of this equation involves the product logarithm. But important properties can already be seen by solving the equations for the power $P_0(w)$. It becomes apparent that $P_0(w)$ has a minimum, meaning that there is a minimum power required to fulfill condition (3.7). Additionally it is continuous for $w > 0$. Thus for any power greater than the minimum power

$$\min P_0(w) = P_{min} = e^1 s_0 I_s r_{clip}^2 \pi \tag{3.8}$$

there will be two solutions[3] as depicted in figure 3.10. One will minimize the amount of wasted power and having a high intensity in the center. The other one will produce a flatter profile, but also wastes a lot of power as the available power increases (figure 3.11)

As there is the minimum in $P_0(w)$ there might be no real solution to (3.7), if the laser power in that beam is limited. In this case the capture radius r_{cap} has to be less than r_{clip}in order to get the best performance. The maximum covered cross section/maximum capture radius can be achieved by choosing the waist w_{opt} such that the minimum P_{min} equals the

[3]There is always also one solution with a negative waist, which is equivalent to the one with positive waist.

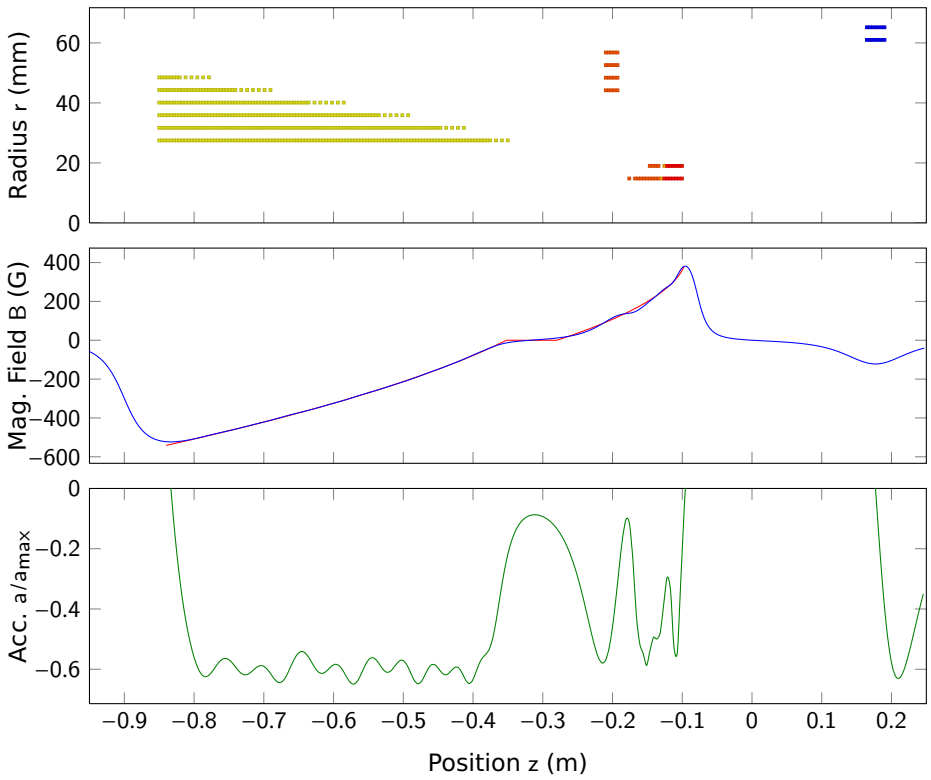

Figure 3.12. Zeeman slower winding pattern, measured magnetic field and calulated acceleration.

available laser power P_0. This leads to

$$w_{\text{opt}} = \sqrt{\frac{2P_0}{\pi e^1 s_0 I_s}} \approx 0.484 \sqrt{\frac{P_0}{s_0 I_s}} \tag{3.9}$$

and a capture radius of

$$r_{\text{cap}} = \frac{w_{\text{opt}}}{\sqrt{2}} < r_{\text{clip}}.$$

3.4.2. Experimental Realization

3.4.2.1. Coils

At the time I joined Markus' group the (first) Zeeman slower was already built[25]. But during the assembly of the vacuum chamber it turned out that the 1 in OD 316 stainless steel tube the decreasing section was wound on had bent under the weight of the copper. This caused the vacuum tube to touch the slower, which would have transferred vibrations

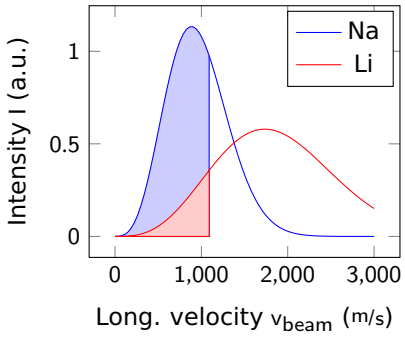

Figure 3.13. Velocities that can the be slowed down by our Zeeman slower with the magnetic field profile described in the text.

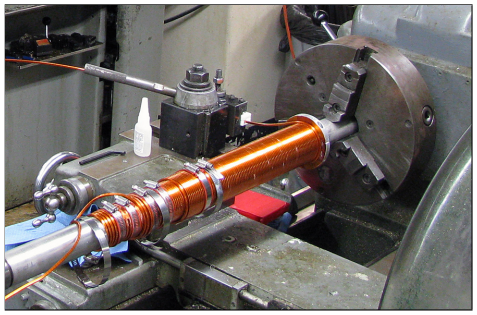

Figure 3.14. Photo of the decreasing field section mounted on a lathe after a few windings.

from the water cooling to the vacuum chamber. In addition the 4 mm outer and 2 mm inner edge square Kapton insulated hollow core wire had almost been used up.

Thus a major redesign of the decreasing section of the spin-flip slower was necessary. The new decreasing section is shorter, is wound on an 2 in tube that even can fit a CF16/1.33 in flange and has fewer layers, but is also using doubly-spaced windings to keep the field smooth. As already for the existing increasing section the magnetic field profile was simulated and manually optimized using a self-written software. The design goal was rather to keep the acceleration constant and lower than $^2/_3 a_{\max}$ than to exactly follow the "ideal" profile.

The whole Zeeman slower is optimized for sodium. The efficiency for lithium is less, but as we need a lot more sodium atoms to sympathetically cool the fermionic lithium atoms later this is fine. The magnetic field the reaches from −500 G to 380 G with a laser 620 MHz red detuned from the cycling transition. The final velocity of the atoms after the slower was designed to be 50 m/s, slow enough to be captured inside the magneto optical trap. Using (3.3) one can estimate the maximum captured velocity to be $v_{\max} = 1090\,\mathrm{m/s}$ (figure 3.13), which results in a capture efficiency of the our slower of 66 % for sodium and 12 % for lithium (without adjusting the currents).

The new decreasing section was wound onto the 2 in OD 316 stainless steel tube that was mounted in a lathe (photo 3.14). During the process the windings where glued in place using PERMABOND 919/920 high-temperature super-glue. In order to make the doubly-spaced windings at the end of each layer three comb-like PFTE spacers had been con-

structed and hold in place with hose clamps, before the wire was again glued in place. After the windings where finished the whole slower was coated with high-temperature epoxy to give more structural stability.

To connect the cooling water to the coil a copper blocks with a round bore on one side with a short piece of pipe and a square bore on the other side for the hollow core wire was machined. This block also has a tapped hole for the electrical connection. In order to make sure the slower can sustain baking temperatures above 200 °C the connections were brazed together and the connector blocks were mounted to a hybrid PTFE/aluminum structure. But it turned out that even during the baking the leads and the connectors stay reasonable cold so that the easier to handle normal "low-temperature" solder could have been used.

3.4.2.2. Slower Light and Optics

Our Zeeman slower operates 620 MHz red-detuned of the sodium D_2 ($3^2S_{1/2} \rightarrow 3^2P_{3/2}$) cycling transition $|F = 2, m_F = 2\rangle \rightarrow \left|F' = 3, m_F = 3\right\rangle$. Due to off-resonant excitation followed by decay into the "wrong"/"dark" hyperfine ground state $|F = 1\rangle$ a repump light, pumping the atoms back into the bright $|F = 2\rangle$ ground state.

Because of the different g_j of the dark state the Zeeman shift of the repump transition differs from the one of slowing transition. Hence it is repump detuning compared to the slowing beam effectively varies along the Zeeman slower. In our design the repump is resonant to the $|F = 1\rangle \rightarrow \left|F' = 2\right\rangle$ transition only in the zero field section with a detuning from the cycling transition (in a field free region) of 1.713 GHz.

To be able to achieve the proposed deceleration of $a = {}^2/_3 a_{\max} = s_0/(s+1) \cdot a_{\max}$ a saturation parameter of at least $s_{0,\min} = 2$ is required, but as a precaution $s_0 = 3$ was chosen. Altogether our laser power budget allows the Zeeman slower beam to have at most a power of 60 mW.

Using geometric optics approach for the atomic beam it turns out that the limiting aperture is the inner diameter of the Zeeman slower vacuum tube close to the main chamber. But equation (3.8) shows that the available power is not enough to overfill the aperture enough to fulfill condition (3.7). Instead the beam waist is chosen according to formula (3.9) $w_{ZS} = 6$ mm. For the first tests we have been using a collimated beam with this waist, but we plan to use a beam that still has this waist at the MOT locating but is focused towards the nozzle. Together with the end of the second differential pumping tube (0.18 in ID) as the second defining aperture and waist of $w_{\text{dpt}} = 1.7$ mm there, we have to start with a waist on the Zeeman slower window of $w_{\text{wnd}} = 10$ mm and focus it 2.6 m away (which coincidentally

is roughly the location of the nozzle). The focusing is done with a defocused ×10 telescope build from achromatic lenses (10 mm and 100 mm from THORLABS) to have good performance both for the sodium and lithium beams. The optics for slowing the lithium atoms will be designed once we gained more experience with sodium.

The vacuum window through which the Zeeman slower beam enters the chamber is directly exposed to the atomic beam. It turned out [26] that the coating of the alkali atoms can be prevented by heating the glass continuously to 200 °C. In our experiment this is achieved by an oven constructed from an aluminum tube that is clamped to the CF40/2.75 in flange of a Housekeeper sealed (glass-to-metal transition) viewport from LARSON. The open end is sealed with an AR-coated 2 in BK7 window from CVI/MELLESGRIOT mounted to a proper adapter piece. The whole assembly is heated from the outside using an OMEGA heater tape and temperature stabilized using the same system as our oven heaters. Six thermocouples monitor the temperature on the inside of the oven in different places.

The outgassing of heated vacuum parts increases our pressure inside the dump chamber by about $2 \cdot 10^{-11}$ Torr. Probably a coldfinger or just cooling the chamber slightly further upstream might help. In addition the atomic beam also increases the pressure by the same amount, but it drops back immediately when the beam shutter is closed.

Another problem that we experience is that some outgassing inside the viewport oven condenses on the AR coated (outer) window and coats it with a very thin sticky layer. The most probably candidate is the silicone glue of the high-temperature Kapton tape used to hold the thermocouples in place. This will be addressed the next time the atomic beam oven is shut down completely.

3.5. Main Chamber

3.5.1. Body

The design goal for this main chamber was to have an inexpensive vacuum chamber optimized for fast evaporation in a quadrupole trap. Optical access is not of great importance as the actual experiment is going to happen in the science chamber.

In order to create strong magnetic field gradients in the quadrupole trap the distance between the coils d should ideally be equal to the radius (anti-Helmholtz configuration). This can be seen by the fact that the gradient of the on-axis magnetic field in the center between to current loops with radius R and spacing d carrying to opposite currents $I_{\pm}$ =

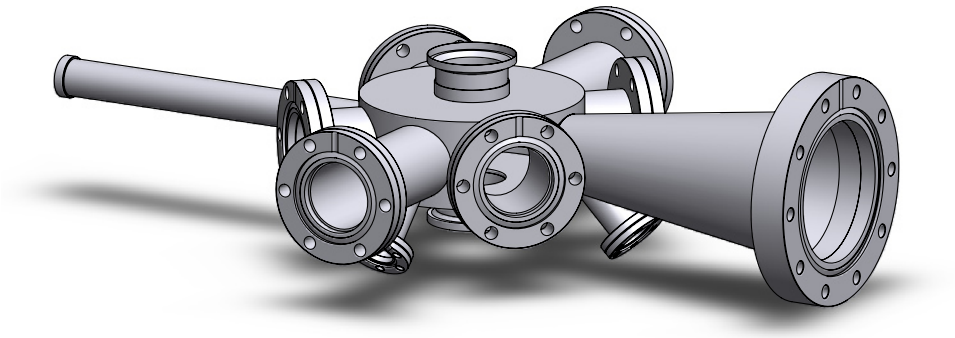

Figure 3.15. Three dimensional model of the main chamber.

$\pm nI_0$ decays with

$$\left.\frac{\partial B}{\partial z}\right|_{z=0} = \frac{48\mu n I_0}{25\sqrt{5}R^2}\left(1 - \frac{4}{R^2}(d-R)^2 + \mathcal{O}\left((d-r)^3\right)\right)$$

around its optimal value of $d_{\text{opt}} = R$.

In our design the lower boundary for the distance is given by outer diameter of the MOT and transport tubes. Those, in turn, are supposed to have a sufficient inner diameter not to clip the MOT beams. Having this in mind a possible solution was to use CF40/2.75 in flanges together with 1.5 in OD/1.35 in ID. The resulting outer diameter of the main body of the chamber of 4.5 in is convenient because this size is also a standard size for vacuum tubes and thus reasonably cheap.

3.5.2. Pumping

As there is no pump directly attached to the main chamber, it was important to have a high conductance connection to the dump chamber, where the actual pumping is happening. The conductance of a tube with diameter of d and length l scales with

$$C \propto \frac{d^4}{l}$$

in the molecular/ballistic regime. Thus it is important to keep the connection short and with a large cross section. The biggest inner diameter with a reasonable flange size was found to be a conical reducer, reducing from 3 in down to the 1.5 in tube that is welded to the main chamber body. This leads to the rather unconventional flange size of CF 4.625 in.

3.5.3. Viewports

For optical access along the vertical direction the top and bottom have welded non AR coated viewports. All the other viewports are CF flanged viewports from LESKER with AR coating for 532 nm, 589 nm, 670 nm and 1064 nm. Except those horizontal viewports having 304 flanges, the whole main chamber was welded from 316 stainless steel parts only. The reasons for that are the superior magnetic properties, which are crucial for the magneto optical transport. The downside of keeping everything non-magnetic is that the viewports have lead alloy seals, which limits the maximum bakeout temperature to 200 °C compared to Kovar sealed viewports.

If I was to redesign this chamber, I would use Housekeeper sealed viewports for the vertical direction to have the possibility to pre-bake to 400 °C.

3.5.4. Antennas

An additional challenge was to get the microwave and rf required for the evaporative cooling into a steel chamber that acts to some extend as a faraday cage. At the desired frequencies (1.77 GHz for sodium and 228 MHz for Lithium respectively) the TEM modes are not even supported by the dimensions of the chamber. Our approach is to have two antennas inside the vacuum chamber close to the atoms. The leads should be kept as short as possible to avoid self-resonances below the 1.77 GHz.

Some quantitative preliminary test showed that having a single loop antenna with ≈ 1 in diameter for the microwave and double loop antenna of the same diameter for the radio frequency should be able couple enough power to the atoms. The antennas consist of 50 mil copper wire that has been etched in 30 % hydrochloric acid. They are connected with in-vacuum barrel connectors (LESKER FTAIBC058) to a separate 2-pin electric feedthrough (LESKER EFT0123052). The wire is insulated with 0.10 in OD ceramic beads. Inside the 0.75 in OD vacuum tube there was one additional layer of 0.26 in OD ceramic beads necessary to prevent the barrel connectors from shorting to the chamber walls. The feedthroughs are mounted on CF16/1.33 in flanges that are sitting on 0.75 in OD vacuum tubes welded in 45° from transport and Zeeman slower axis repectively (see figure 3.15).

The 1 in diameter loops cannot be inserted through the 0.75 in vacuum tubes. Hence the have to be inserted through a viewport or the large reducer. Then the leads can be pulled out from the CF16 flanges and connected to the feedthrough. This procedure is a bit tricky and it took as several tries to have the antennas where we wanted without shorting it to the chamber.

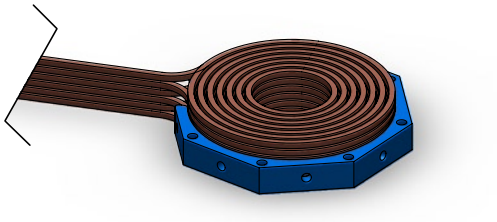

Figure 3.16. Three dimensional model of the main chamber quadrupole coil including the mounting clamp.

3.5.5. Quadrupole coils

Our design goal was to generate a magnetic field gradient of approximately 500 G/cm allowing us to do a fast RF evaporation in the trap. As already mentioned in section 3.5.1 the minimum distance between the coils is given by the size of the chamber. In addition the total height of the coil pair should be as small as possible, because otherwise the distance between the transport coils (see chapter 6) would require a large current for reasonable confinement during the transport. This limits the total number of layers for the quadrupole coil.

In order to effectively cool the coil, it is made out of square 4 mm lateral length and a 2.5 mm diameter bore hollow core copper wire with fiberglas insulation. Two layers with 7 windings each are wound from a single wire each to a "two layer pancake". Each coil consists of three such pancakes and is molded into a single block with epoxy together with thermocouples to monitor the temperature of the coils. As each pancake has separate leads and the cooling water is connected in parallel, the coolant flow is higher than just all layers in series. Winding such pancake pattern with a hollow core wire is hard, because of its tendency to twist by 45° for smaller radii. To safe us some trouble we had our coils made by OSWALD in Germany. The overall quality was good, but the winding itself could as well been done by us. Another disadvantage is that they used ARALDITE F epoxy which cannot be baked.

To mount the coils we designed a C shaped clamp that is epoxied to the molded coil blocks. The slotted design reduces eddy currents that are created by fast switching of the currents and thus limiting the turn-on/off time of the magnetic fields. On the inside there are milled grooves to facilitate a strong bond between the clamp and the epoxy.

3.6. Laser and Optics Setup

3.6.1. Sodium Laser

3.6.1.1. Source

At the time of this work they only reliable way of getting resonant light for the sodium D_2 transition at 589 nm with sufficient power (> 1.5 W) is using a dye laser. Dye lasers are known to be "care intensive". But at the time of this work the only alternative, the solid state laser using sum frequency generation from two Nd:YAG lasers at 1064 nm and 1319 nm[27], was not yet working reliable enough for us to consider it as an alternative. Another option might be a frequency doubled fiber laser that is currently developed by TOPITICA.

We used a SIRAH Matisse Dye Laser (converted from a Matisse Titanium Saphire Laser) to produce the 589nm light for sodium. It's pumped by a Coherent Verdi V18 at 15W. As dye we are using 3.2 g EXCITON Rhodamine 590 Chloride dissolved in 4 l of ethylene glycol.

The cooling that is provided by the heat exchanger dye tank of the Sirah pump was not sufficient to keep the dye temperature low enough. Thus we first could not use a higher pressure than 15 bar without having bubbles in the dye return line. This was most likely caused by the higher viscosity of the warm glycol and our cooling water alone (18 °C) was not able to cool the dye enough.

So we designed two water cooled Peltier cooling blocks consisting of four TE TECHNOLOGIES HP-199-1.4-08PR TECs each. In addition we insulated the dye tank and the overflow reservoir using foam. Especially the insulating the tank made a great improvement as the pump itself sitting directly below the tank created a lot of heat (≈ 400 W heat dissipation), which again heated the dye.

With the cooling block running at full power we were able to cool the dye below 10 °C. In the experiment we found that 350 W resulting in a temperature of 15 °C is sufficient to reliably allow higher pressure of 16.5 bar without overloading the pump due to the low viscosity of cold dye. All the dye temperatures have been measure inside the overflow dye reservoir with an OMEGA infrared thermometer.

In future we hope to reduce the dye concentration in order to reduce the thermal lensing in dye and thus making even higher output powers possible.

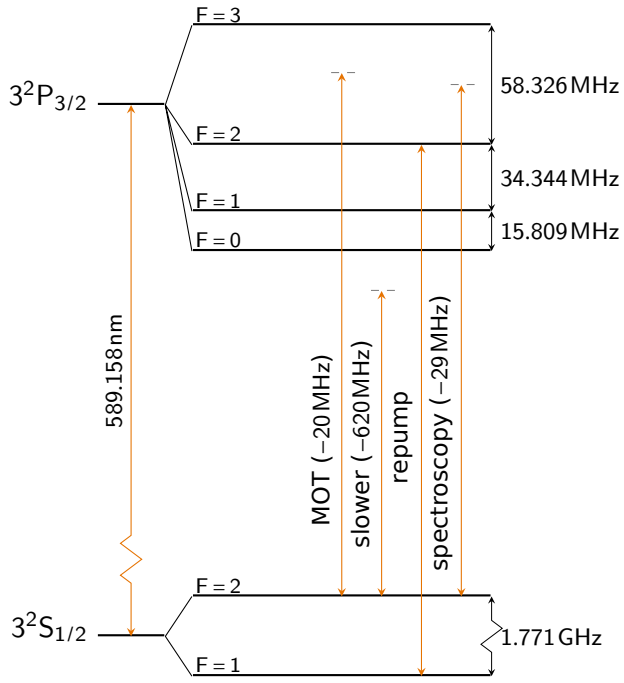

Figure 3.17. Energy levels of sodium and the transitions used in our experiment. The detunings are in respect to the cycling transition $|F = 2\rangle \rightarrow |F' = 3\rangle$. (Sodium data from [28])

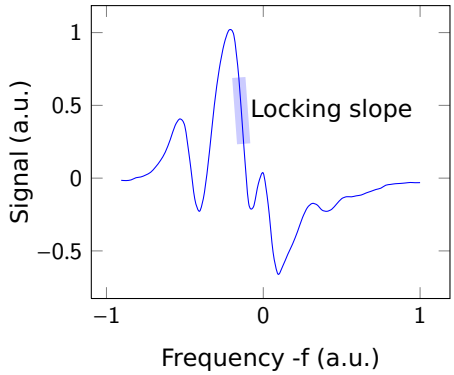

Figure 3.18. Measured dispersive spectroscopy signal from our sodium FM spectroscopy setup.

3.6.1.2. Locking

Our dye laser is frequency locked 249 MHz red-detuned from the sodium D_2 ($3^2S_{1/2} \rightarrow 3^2P_{3/2}$) cycling transition $|F=2\rangle \rightarrow \left|F'=3\right\rangle$. To achieve the lock it is first locked to temperature stabilized cavity from SIRAH with a Pound-Drever-Hall lock[29]. This lock has a high-bandwidth and activley reduces the laser bandwidth to several 100 kHz. The cavity in turn is locked by a slow software PID servo loop to a sodium spectroscopy setup.

The frequency modulation (FM) spectroscopy[30] is done with the usual double-pass setup in a sodium reference cell heated to 170 °C. Higher temperature give better signal-to-noise ratio (especially in the Doppler-free DC signal), but the pressure broadening prevents resolving the hyperfine states in the spectrum. The crossover resonance of the $|F=2\rangle \rightarrow \left|F'=2\right\rangle$ and $|F=2\rangle \rightarrow \left|F'=3\right\rangle$ lines is chosen for the lock, because it gives the strongest signal in the dispersive (AC) signal (figure (3.18)).

3.6.2. Lithium Laser

The laser light for the Lithium transitions is generated by two 670 nm laser diodes. One of them seeds a tapered amplifier that again seeds two tapered amplifiers with a maximum output power of 500 mW each. A detailed description of the laser system for Lithium can be found in [25].

4. Making the two-species MOT

4.1. Motivation

Although the atoms are already cooled a lot compared to the initial temperature, they still have a temperature of about 3 K in the beam direction[1]. In order to reduce the temperature by about six more orders of magnitude to the critical temperature of the Bose-Einstein condensation, additional cooling mechanisms are necessary. The first step for this is (in almost all BEC experiments) the magneto optical trap (MOT). The magneto optical trap first discovered in 1987 by [31] is *the* workhorse of cold atom experiments. It even solves two problems at once: trapping and cooling.

4.2. Theory

4.2.1. Trapping and Cooling

The MOT, similar to the Zeeman slower, uses the radiation pressure in combination with magnetic field gradients to push the atoms towards the center of the trap and cool them. The principle of the MOT can best be understood in the one dimensional case for a atom with total angular momentum $J_g = 0$ in the ground state and $J_e = 1$ in the excited state (but works for all $J \rightarrow J+1$ transitions in a similar fashion). The magnetic field is to be assumed to have a constant gradient: $B(z) = Az$. This leads to a position dependent Zeeman shift of the magnetic sublevels (figure 4.1) and thus introduces a position dependent detuning $\delta_\pm(z)$ of the two counterpropagating red detuned laser beams ω_L from the atomic transisiton frequency ω_A. In addition the two circularly polarized beams also have opposite polarization $\sigma_\pm$ with respect to the quantization axis (z axis in this case). So an atom at $z < 0$ will feel the force of the radiation pressure $\mathbf{F}_\pm$ from both σ_+ and σ_- beams, but the σ_+ is closer detuned

$$\delta_+(z) < \delta_-(z)$$

[1] Strictly speaking one cannot define a temperature as the slowed down atoms are not in a thermal equilibrium.

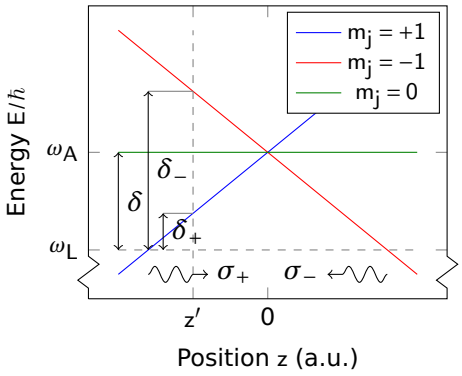

Figure 4.1. One dimensional configuration of a magneto optical trap for a fictional two-level atom with $J_g = 0$ in the ground state and $J_e = 1$ in the excited state.

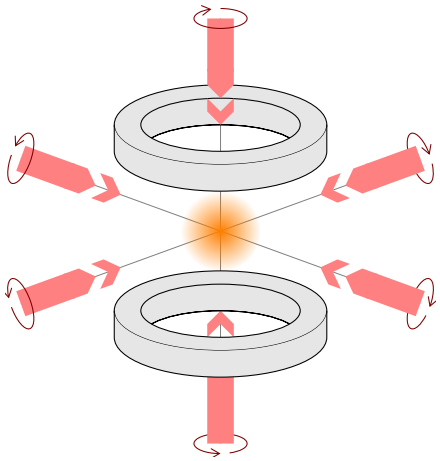

Figure 4.2. Helicity of the MOT beams in a three dimensional configuration. The coils are in anti-Helmholtz configuration and produce a quadrupole field.

and thus pushes it towards the center of the trap. Note that the confinement is dominated by the light forces. Magnetic confinement can be neglected at the typical magnetic field gradients.

This trapping and cooling scheme can easily be extended into three dimensions. The magnetic field gradient then is produced by a pair of coils in anti-Helmholtz configuration (figure 4.2). The confinement is generated of six pairwise counterpropagating laser beams with opposite polarization (same helicity) in respect to their common axis.

If one now takes the Doppler shift of the finite velocity into account, it follows from equation (2.5) that the forces are given by

$$\mathbf{F}_{\pm} = \pm \frac{\hbar \mathbf{k}_{\mathrm{L}} \gamma}{2} \frac{s_0}{1 + s_0 + \left(2\delta_{\pm}(\mathbf{x}, \mathbf{v})/\gamma\right)^2}, \tag{4.1}$$

where the effective detuning is given by

$$\delta_{\pm}(\mathbf{x}, \mathbf{v}) = \delta \mp \mathbf{k}_{\mathrm{L}} \cdot \mathbf{v} \pm \frac{\mu}{\hbar} B(\mathbf{x}).$$

As already for the theory of the Zeeman slower μ is the effective magnetic moment (see equation (3.2)). In the limit of small displacements from the trap center ($\mu A x/(\hbar\delta) \ll 1$)

and small velocities ($k_\mathrm{L} v/\delta \ll 1$) in the form

$$\mathbf{F} = \mathbf{F}_+ + \mathbf{F}_- = -\kappa \mathbf{x} - \alpha \mathbf{v} \tag{4.2}$$

with

$$\kappa = \frac{\mu A}{\hbar k_\mathrm{L}} \alpha$$

and

$$\alpha = -8\hbar k_\mathrm{L}^2 \frac{s_0(\delta/\gamma)}{\left(1 + s_0 + (2\delta/\gamma)^2\right)^2}.$$

As already for the Zeeman slower the combination of Zeeman and Doppler shift leads to a dissipative force.

The point where this approximation breaks down, i.e. the force is not linear in the velocity, also defines the *capture velocity* of the magneto optical trap.

$$v_\mathrm{c} \sim \frac{\delta}{k_\mathrm{L}}$$

This is in rather bad agreement with the real capture velocity that only can be found in numerical simulations. For sodium and a detuning $\delta = -2\gamma$ this velocity would be $v_\mathrm{c,Na} = 12\,\mathrm{m/s}$.

The corresponding equation of motion of equation (4.2) is a classical damped harmonic oscillator governed by following differential equation:

$$\ddot{\mathbf{x}} + 2\beta\dot{\mathbf{x}} + \omega_0^2 \mathbf{x} = 0 \tag{4.3}$$

with the frequency $\omega_0 \equiv \sqrt{\kappa/m}$, damping $\beta \equiv \alpha/(2m)$ and the mass m of the atom. For typical trapping parameters of a sodium MOT with $\mathrm{d}B/\mathrm{d}z = 10\,\mathrm{G/cm}$, $\delta = -2\gamma$ and $s_0 = 1$ this motion is overdamped with $\omega_0 = 3.6\,\mathrm{kHz}$, $\beta = 7.8\,\mathrm{kHz}$ and a corresponding time constant of $\tau = 2\beta/\omega_0^2 = 1.2\,\mathrm{ms}$.

Equation (4.3) implies that one can reach absolute zero temperature with Doppler cooling. But the used model lacks a small detail: although the spontaneously emitted photon is uniformly distributed over 4π, it kicks the atom with a recoil momentum $\hbar k_\mathrm{L}$ and thus leads to a random walk through the phase space. This in turn broadens the velocity distribution. It can be shown that for low intensities this gives rise to a lower temperature limit of

$$k_\mathrm{B} T = \frac{\hbar\gamma}{4} \frac{1 + (2\delta/\gamma)^2}{-2\delta/\gamma}.$$

The smallest temperature in this model can be achieved with $\delta = -2\gamma$. This defines the so-called *Doppler temperature* T_D

$$k_B T_D = \frac{\hbar\gamma}{2} \tag{4.4}$$

For the sodium D_2 line this results in a temperature of $240\,\mu$K. Additionally it can also been show that this diffusion also leads to a Maxwell-Boltzmann distribution inside the trap making defining a temperature possible.

In experiments the temperature often is found to be lower than this theoretical limit. This is due to a sub-Doppler cooling mechanism called *optical molasses*. It is a Sisyphus-type cooling scheme that uses the polarization gradient produced by the counterpropagating MOT beams and doesn't rely on the scattering of photons, but uses the dipole force instead. Usually BEC experiments do optical molasses cooling in a separate step after loading the MOT by switching off the magnetic fields and changing the detuning of the lasers. But Wolfgang Ketterle's experiments at MIT have found that for a sodium BEC with a huge atom number the optical density is too high and molasses cooling doesn't work very well. Because of this optical molasses cooling won't be discussed further in this work.

Repumping Because the magneto-optical trapping beams are detuned from resonance there is some mixing with other excited states. This leads to a non-zero probability to end up in the "wrong" hyperfine state of the lower state of the cooling transition. Atoms in this state are not resonant to the MOT beams and would accumulate in this dark state. To prevent this an additional laser (or just side bands on the trapping beam) is tuned in such a way that the atoms get pumped back into the correct "bright" hyperfine state.

4.2.2. Losses and the Dark-SPOT

There are several factors that limit the maximum density (around $10^{11}\,\mathrm{atoms/cm^3}$ for conventional MOTs[31]) and thus the total number of atoms captured inside a magneto optical trap.

First at higher densities two-body losses start to occur due to the increasing scattering rate. For alkali in a magneto optical trap the main contribution comes from inelastic collisions of atoms in the excited state and atoms in the ground state. The collision can be finestructure-changing for the excited state ($P_{3/2} \rightarrow P_{1/2}$) and thus release a energy on the order of 10 K per atom[32].

$$A + A + \hbar\omega \rightarrow A + A(P_{3/2}) \rightarrow A + A(P_{1/2}) + \Delta E_{FS}$$

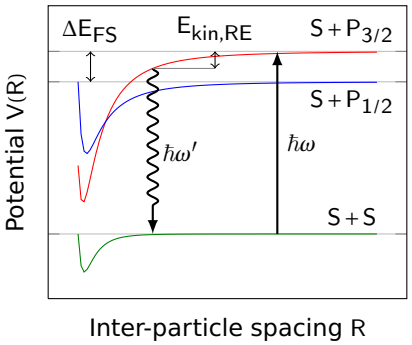

Figure 4.3. Potential curves for different combination of ground state (S) and excitate state ($P_{1/2}$, $P_{3/2}$) collisions. The released energy for both finestructure changing (ΔE_{FS}) and radiative escape ($\Delta E_{kin,RE}$) loss processes is visualized[32].

The atoms cannot be trapped anymore and escape the trap. The hyperfine-changing collisions between two ground state atoms release less energy than the trap depth and are not of great importance in a MOT.

In addition to those two state-changing collisions, energy can also be released in a process called *radiative escape*. Because of the low temperatures the collision time can be on the order of the lifetime of the spontaneous emission. When the emission happens during the scattering (the two atoms form a long-ranged quasi-molecule due to attractive dipole-dipole interaction) the emitted photon is red detuned from the atomic transition and hence releases kinetic energy of $\hbar(\omega-\omega')/2$ per atom (visualized in figure 4.3)[33].

$$A + A + \hbar\omega \rightarrow A_2^*(P_{3/2}) \rightarrow A + A + \hbar\omega' + E_{\text{kin}}$$

The total two-body loss rate of these three processes is proportional to the density βn, where the constant β is on the order of $10^{-11}\,\text{cm}^3/\text{s}$[34].

The second limitation to the maximum density is the reabsorbtion of spontaneously emitted photons inside the MOT (*radiation trapping*)[35, 36]. This leads to an outwards directed radiation pressure that is in competition with the radiation pressure of the trapping beams. If one loads more atoms in the trap, the density stays constant. Intuitively one would expect Gaussian density distribution assuming an ideal gas in a harmonic trapping potential, but this is only true for low density MOTs, when the reabsortion can be neglected.

This effect can be estimated in a simple model[37]. Instead of assuming a simple two-level atom, one introduces an additional *dark* state that can only be pumped by an additional repump beam back into the *bright* state. With the probability p_{bright} that an atom

resides in the bright state, the steady-state trapping force is given by

$$F_{\text{trap}}(r) = -kp_{\text{bright}}r,$$

where k denotes the spring constant (related to κ in the previous section) of the trap and r the distance from the trap center. The outwards directed radiation pressure is accounted by

$$F_{\text{rad}}(r,n) = +k\frac{n}{n_0}p_{\text{bright}}^2 r.$$

It is quadratic in p_{bright} because there are two absorption processes involved, n_0 is some normalization constant. For the MOT to be stable it is required that

$$F_{\text{trap}} > F_{\text{rad}}$$

and hence

$$n < n_0 / p_{\text{bright}}.$$

So in order to increase the density in the MOT the amount of time in the bright hyperfine state has to be reduced. But there also certain limitations to choosing p_{bright} too small, like an increasing volume due to a decrease in the confining force. The ideal value is predicted to be around ≈ 0.01[37].

Ketterle's approach is to have a dedicated repump beam with a circular area in the center with zero intensity, the so called *dark-SPOT*. Thus atoms in the center of the trap are not being repumped back to the bright state and effectivley stay dark. Active depumping into the dark state was shown by [38] for rubidium.

Another loss mechanism in MOT that has not been mentioned yet, collisions with the hot (room temperature) background gas. The rate is independent und thus shows as an exponential decay of the atom number. It only depends on the vacuum pressure. With a 10^{-11} Torr pressure lifetimes of many 100 s are possible.

In general the figure of merit for a magneto optical trap is the product of the density and the trap lifetime $n\tau$. In order to have a higher absolute atom number one "just" has to increase the size of the MOT beams while keeping the intensity constant.

4.3. Experimental Realization

Sodium The laser light for the MOT setup is transmitted through polarization maintaining single mode fibers to the two vertical $24 \times 18 \times 0.75$ in aluminum breadboards. Every single fiber exit port has a polarizing beam splitter to clean up the polarization and is has a feedback photo diode in order to servo the intensity. We tried several different solutions to get a beam with 0.5 in waist (1 in diameter) without (especially spherical) abberrations. An acceptable solution was obtained by using THORLAB's fixed focal length fiber outcouplers F240-TME-A/B and a $1:2$ telescope to pre-expand the beam to 2.5 mm diameter, before the two colors get mixed on a dichroic mirror and get expanded to the final beam size using a $1:10$ telescope. Our setup is especially space efficient as always cross/overlap two MOT orthogonal $1:10$ telescopes. The large diameter MOT beams will allow us to trap a larger number of sodium atoms even if we reach the density limit.

A difference to a lot of other MOT setups is that we do not retro-reflect the beams. The transmitted beam has a hole due to the high optical density of the sodium MOT. Thus we are using six separate beams for trapping for each species. In order to combine the beams with other beams like imaging, optical pumping and dark-SPOT repump, each of this six beam paths has a 2 in polarizing beamsplitter cube, where an orthogonal polarization can be mixed. One such path is shown in figure 4.4.

The initial alignment of the magneto-optical trap will be done in a "bright" MOT, where the repump light is mixed as sidebands onto the cooling light by an EOM. The detunings are given in figure 3.17. At the time of this work we've just trapped our first sodium atoms in the MOT (figure 4.5)! On this picture one can also see the fluoresence of the atomic beam. The atoms in the beam can absorb the photons from the vertical MOT beams, because the beam is cold in the radial direction. After the "bright" MOT is optimized, we are going to implement the dark-SPOT by having a dedicated repump beam that casts a shadow at the center of the trap.

Lithium An additional challenge will be to add the second species MOT, lithium, to the setup. The laser setup is already described in [25]. The main difference for lithium is that the difference between cooling and repump light vanishes, because the hyperfine states overlap due to the small splitting compared to the natural linewidth. Thus the cooling and repump beams have almost equal intensity.

The problem with having a two-species MOT is that light assisted interspecies collisions can increase the loss rate [39, 40]. To reduce this effect the two traps are going to be spa-

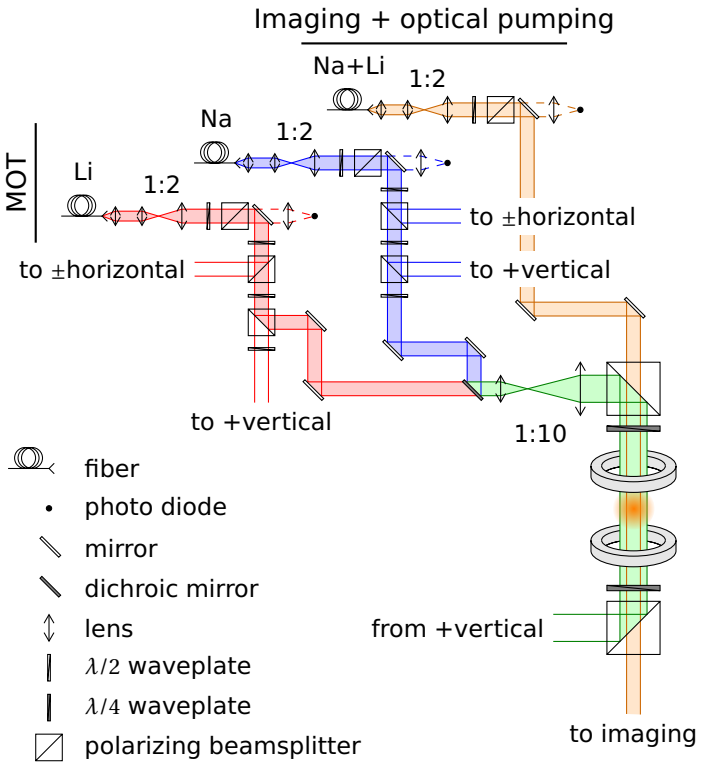

Figure 4.4. A part of the optics setup for two-species MOT. All horizontal trapping beams are omitted.

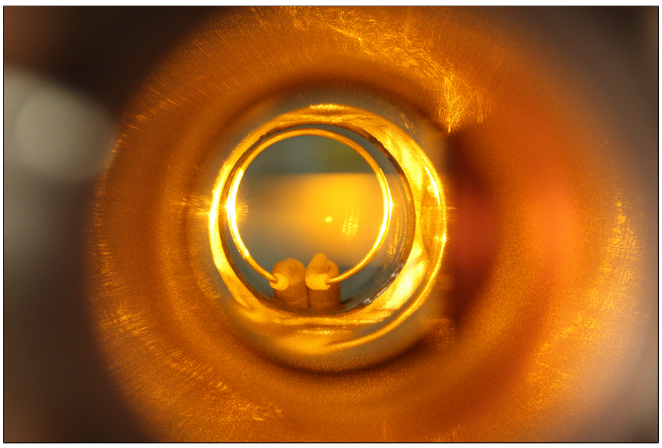

Figure 4.5. The reward for all the hard work: the first glimpse on our sodium MOT sitting in the flourescing atom beam. The coil in the background is the antenna for RF evaporation.

cially separated by displacing the lithium MOT a few millimeters from the magnetic field center[41]. At the end it will be a compromise between atom number in both MOTs and transfer efficiency into the magnetic trap for evaporation. For example if the MOT is too far off-centered from center the magnetic trap heating due to center of mass motion (sloshing) can occur.

5. Towards the Sodium BEC and the Lithium DFG

Once the two-species MOT is going to be set up a few more things have to be implemented in order to achieve quantum degeneracy both in sodium and lithium. The two clouds in the magneto-optical trap are loaded into a plugged magnetic quadrupole trap. Magnetic quadrupole traps have a field zero in the center. Atoms could change their spin-state there and thus jump from a trapped low-field seeking state into the anti-trapped high-field seeking state (Majorana losses). This gets more and more severe as the atoms get colder. In order to prevent the Majorana spin-flips we focus a blue-detuned (532 nm) laser beam into the center of the magnetic trap[42, 43]. The repulsive dipole force will prevent the atoms from entering the zero field region. Because of its lighter mass and smaller linewidth lithium requires higher power (around 8 W) than in a pure sodium experiment.

To cool the atoms further down in a single species experiment usually RF induced evaporation is applied. The fast atoms that can reach regions with higher magnetic fields get "evaporated", i.e. spin flipped into the non-trapped state, by an external RF field (see figure 5.1). The gas then thermalizes again by elastic collisions in the trap. What might not be obvious first is that one actually gets *two* separated condensates for a nicely aligned plug

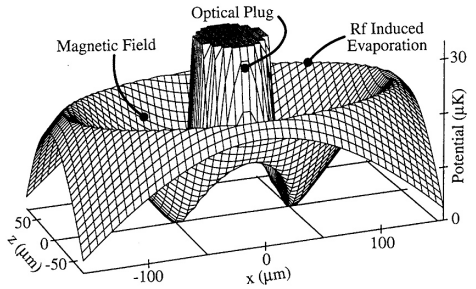

Figure 5.1. Potential created by RF induced evaporation in an optically-plugged quadrupole trap.[42]

beam along the radial direction of the quadrupole coil pair. For a plug beam along the axis of the coils one would get a ring shaped condensate.

This method does not work in a two-alkali-species machine because it only relies on the Zeeman splitting, which is the same for lithium and sodium in the *s* state. So in order to only evaporate the sodium the ground-state hyperfine-transition has to be driven with a 1.77 GHz microwave. The lithium is not evaporated at all, but only sympathetically cooled by collisions with the sodium. A good description together with the choice of the correct spin states is given by [26].

6. Magneto-Optical Transport

6.1. Introduction

The optics required for trapping and cooling the atoms in a magneto-optical trap together with the gradient coils for magnetic trapping and RF evaporation obstruct a lot of the optical access. This restricts the possible experiments and for example hinders adding a 3D optical lattice (although it can be still possible).

Different methods to circumvent these limitations have been established. One is to mechanically move the MOT optics away (translation stage, flipper mirror, etc.) and then use the MOT axis for lattice beams. In addition the gradient coils for evaporation can be avoided by performing all optical trapping and evaporation with focused high power laser beams. The disadvantage of this method is that it is limited to lower atom numbers due to a smaller trap volume compared to magnetic traps and worse mode overlap with the magneto-optical trap. Our approach is to have a dedicated UHV chamber for the actual experiment that requires no MOT optics and/or no coils for magnetic trapping at all.

The challenge now is to transport the atoms from one vacuum chamber into another. Several approaches have been followed. The probably most obvious way is to transport the atoms in a moving magnetic trap. For example this can be achieved by mechanically moving quadrupole coils[44] or generate a moving quadrupole field by switching several quadrupole coils in a row[45]. This method only works for "hot" atoms, because otherwise the Majorana Spin flip losses in the zero field point of the quadrupole field would lead to significant atom loss and heating. Thus it is only possible to transport atoms from a MOT in a low-field seeking state and not a BEC or degenerate Fermi gas (DFG). In addition this method would still need closely placed coils for magnetic trapping in the science chamber.

Hence in order to optimize for a large number of cold atoms one has to already evaporate in the main chamber and then transport the BEC or DFG. This approach bears additional challenges as both are really sensitive to heating. Any fast acceleration on the order of the trap frequency of whatever transport trap violates adiabaticity and increases the temperature. For this ultracold samples with temperatures on the order of $1\,\mu$K and below the

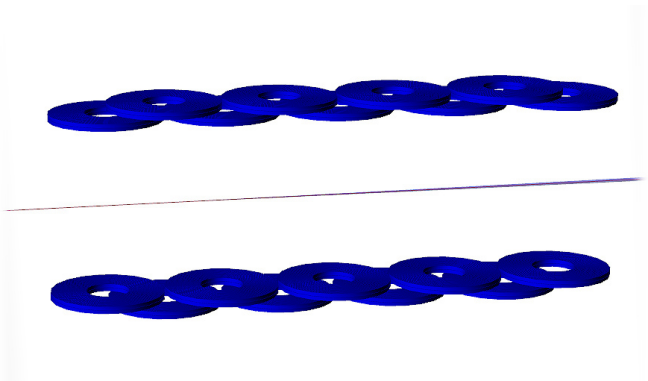

Figure 6.1. Three dimensional depiction of the magneto-optical transport scheme proposed in the text. At least three coil pairs have to carry current in order to keep a constant trap frequency and constant magnetic field.

relative change in temperature is of course more drastic than for example heating of 1 μK in a 300 μK cloud in a quadrupole transport.

A group in Innsbruck [46] moved a BEC in a standing wave optical conveyor belt. But loading a BEC into multiple sites and recombining it afterwards is not trivial and leads to losses. A more common approach is to transport a BEC/DFG in an optical dipole trap by moving its focus[47]. The problem here is that in order to have high trap frequencies even in the longitudinal (transport) direction, the beam has to be tightly focused to several 10 μm. This greatly reduces the trapping volume and thus the total number of atoms, especially for a DFG as it is rather big due to the Fermi-pressure.

6.2. Novel Transport Scheme

We propose a novel magneto-optical transport scheme that could overcome these limitations of the purely optical transport. For the transverse confinement we still use a far red detuned (1064 nm) laser beam. But it does not need to be focused anymore. Ideally it is collimated all the way along the transport.

The longitudinal confinement is provided by a magnetic field. In contrary to the existing quadrupole transport schemes the coils are in *symmetric* configuration (currents flowing in the same direction) and the atoms re in the *high-field seeking* state. Maxwell equations forbid a field maximum in three dimensions, but a maximum in two dimensions is allowed. In fact the field in the center between the two coils has a saddle point, i.e. minimum in the axial direction and a maximum in the radial direction of the coils. But that is alright as

we have the laser beam to provide the confinement in that direction. In order to push the ultracold cloud along the “tube of light” one has to place several coils along the transport and switch them on and off one pair after each other (or even more sophisticated transport ramps). The proposed geometry is depicted in figure 6.1.

6.3. Heating due to Magnetic Corrugations

6.3.1. Overview

Any acceleration that is too fast for the trapped atoms to follow adiabatically can lead to heating. For that reason we studied the influence of magnetic field disturbances caused by surrounding vacuum components. First measurements of the magnetic fields were carried out, which then were used to estimate the heating during the magnet-optical transport.

6.3.2. Magnetic field measurements

For a quadrupole field offset B-fields lead to a shift of the center position. But in our field geometry the center position is sensitive to external gradients. This can easily be seen by assuming a magnetic field

$$B(x) = -\frac{1}{2}cx^2 + B_0$$

with a given curvature c and some maximum value B_0 and superposing it with a external disturbance field

$$\delta B(x) = ax + \delta B_0$$

with a constant gradient a and some arbitrary offset. The new maximum is shifted by

$$x_{\max} = \frac{a}{c}. \tag{6.1}$$

This shows how important it is to avoid any disturbances in the magnetic transport field. In general one can keep the corrugations small by using non-magnetic materials, i.e. without permanent magnetization and magnetic susceptibility χ close to 0 like 316 stainless steel. But most machining processes like milling or welding disturb the crystalline structure of the metals and thus also change their magnetic properties.

We measured these shifts of the field maximum along the transport direction due to the presence of vacuum parts (main chamber and all-metal gate valve). For this purpose we mounted the parts onto a non-magnetic rail out of extruded aluminum rail, where they

could slide freely along one direction on PTFE sliders. The position was measured using a rack-and-pinion drive with a ten-turn potentiometer. In addition a pair of transport coils was mounted stationarily on the sides of the rail.

In order to measure the magnetic fields a magnetic field sensor was placed in the center of the coils mounted on a long titanium rod. It was oriented such that its sensitive axis was perpendicular to the coil axis and thus measuring a field maximum. To map out the field around this center position we could "wobble" the probe along the tail direction with a stepper-motor. Again the absolute position was resistively measured.

6.3.3. Simulation

Based on these measurements we estimated the heating using a simplified classical model. We considered the one-dimensional movement of a single atom of mass m, magnetic moment μ and is sitting in a harmonic trap produced by the Zeeman shift due to parabolic magnetic field. These assumptions are reasonable as long as the interactions within the actual transported atoms can be neglected. This is especially true for a spin-polarized degenerate Fermi gas.

To simulate the transport process, the maximum of the magnetic field/minimum of the confining potential is following a given transport ramp $x_\mathrm{t}(t)$. In addition to that a position dependent perturbation $\delta B(x)$ in the magnetic field is introduced. This gives rise to the time and position depended magnetic field

$$B(x,t) = \frac{1}{2} c_B (x - x_\mathrm{t}(t))^2 + \delta B(x),$$

where $c_B = \frac{\omega^2 m}{\mu}$ denotes the curvature. Under this circumstances the equations of motion of our model atom is governed by following differential equation:

$$\ddot{x}(t) + \mu \frac{\partial}{\partial x} B(x(t), t) = 0 \tag{6.2}$$

This equation can easily be integrated numerically using MATHEMATICA.

After the transport is finished, i.e. $x_\mathrm{t}(t)$ is constant a temperature is estimated from the maximum kinetic energy the atom has during the oscillations, which is equal to the total energy for any time greater than the total transport time t_t: $t' \gg t_\mathrm{t}$. If one starts with zero

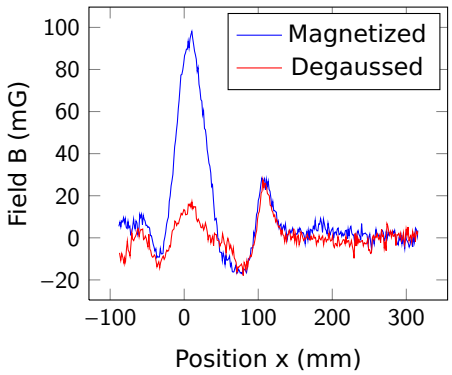

(a) Magnetic field profile of the main chamber without an external field (I = 0) in the magnetized and demagnetized case.

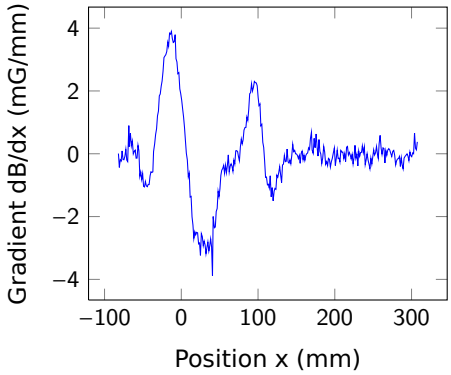

(b) Magnetic field gradients of the main chamber after magnetizing the weld at around x = 30mm.

Figure 6.2. Measurement of the magnetic properties of the main chamber.

temperature, the final temperature gives approximately the total heating

$$k_{\mathrm{B}}\Delta T = \frac{1}{2}m\dot{x}(t')^2 + \mu B(x(t'), t').$$

6.4. Results

6.4.1. Magnetic field measurements

Main chamber We mapped out the field maximum in presence of our main chamber near the weld where the tubes with the CF flanges are connected to its 4.5 in OD body. This relates to the point of $x \approx 30\,\mathrm{mm}$ in plot 6.2a. The flange itself is located at around $x \approx 100\,\mathrm{mm}$. The field profile was fitted to a parabola in order to determine the center. This procedure was repeated for different currents in the magnetic field coils.

The center shift follows roughly the expected $1/c_B$ dependence (the current I is just a scaling factor in the Biot-Savart law and hence magnetic field, gradient and curvature are linear in I):

$$x_0(I) = \frac{28(2)\,\mathrm{mm/A}}{I} + 20.7(2)\,\mathrm{mm}$$

The deviation from the ideal curve in plot 6.3b can be explained by a shift of the field maximum transverse to the transport/wobble direction such that the probe does not hit the *absolute* maximum anymore.

We could also show that the disturbance is dominated by ferromagnetic and not param-

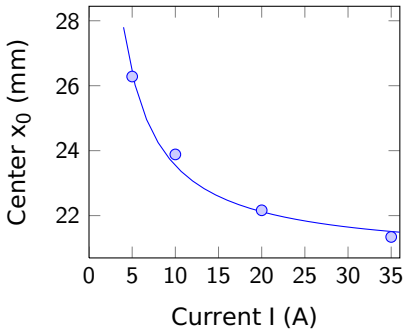

(a) Shift of the center of the magnetic field due to the presence of the vacuum chamber.

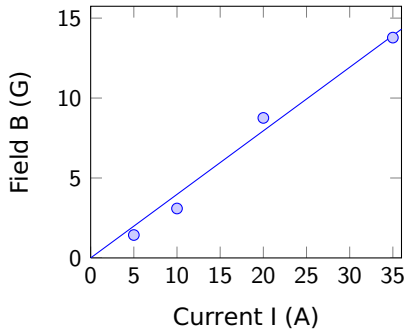

(b) Maximum magnetic field along the "wobble direction" plotted against the current in the coils.

Figure 6.3. Mapping out the magnetic field maximum in the transport direction by "wobbling" a magnetic field probe around the maximum position.

agnetic contributions. The magnetic field probe was moved through the chamber while no external field from the field coils was present ($I = 0$) and the profile was recorded. The center of the chamber resides at $x = 0$. This magnetization could be reversed by "de-gaussing" the weld by driving an additional coil close to the weld with an exponentially decaying AC current. Although the absolute field (plot 6.2a) is small compared to the earth's magnetic field of $B_{\text{earth},\perp} \approx 0.5\,\text{G}$, the gradients (plot 6.2b) are still big enough to cause heating. Our second-generation main chamber was also quickly checked later and the gradients were of the same order of magnitude.

All-metal gate valve In a next experiment we also measured the magnetic properties of our VAT all-metal gate valve, which separates the main and the later science chamber. We decided to perform slightly different measurements instead of the tedious wobble scan. This time we only moved the gate valve while keeping the probe centered in the magnetic field. This is actually closer to the real transport procedure in the experiment.

Again, we saw permanent magnetization on the order of 100 mG in the zero-field case (plot 6.4a). But when we increased the magnetic field ($I = \pm 50\,\text{A}$) additional peaks appeared (plots 6.4b and 6.4c). This peaks gave rise to field gradients (plot 6.4d) exceeding the main chamber by one order of magnitude.

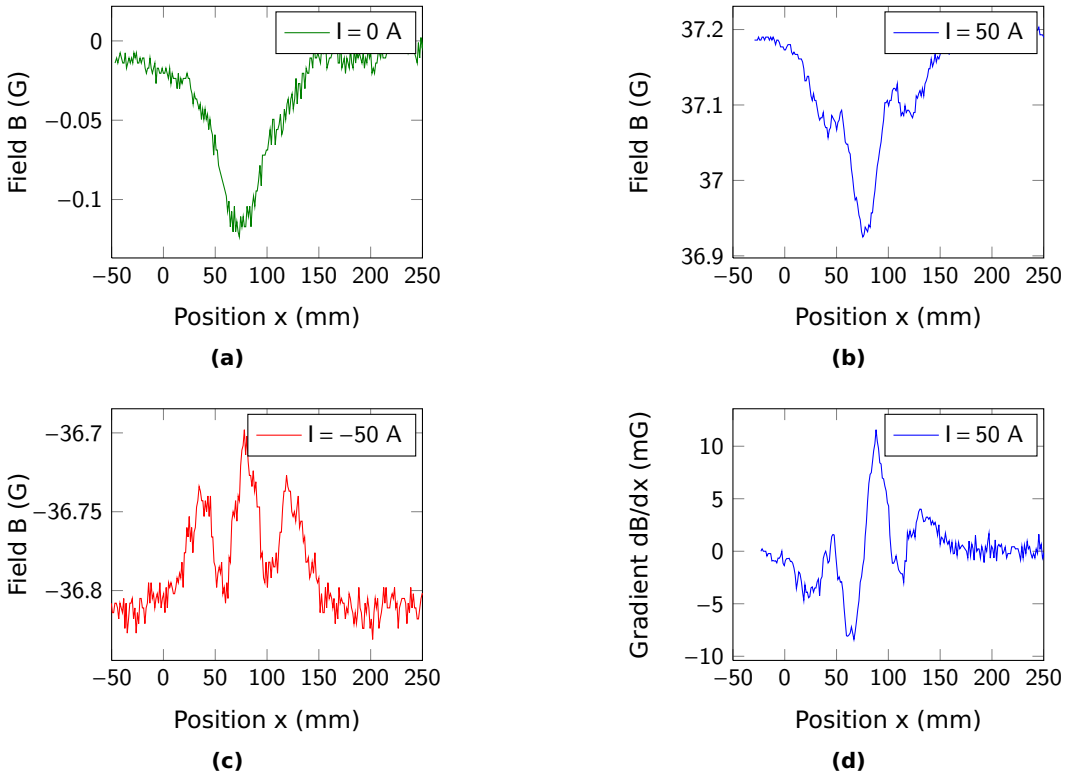

Figure 6.4. Measurement of the magnetic properties of the VAT all-metal gate valve.

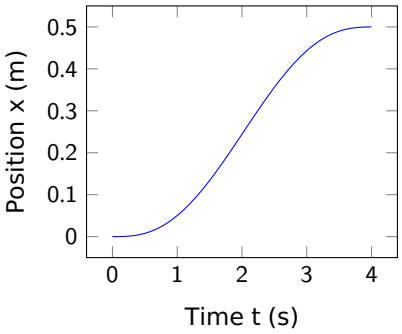

Figure 6.5. Transport ramp used for the simulation with $t_t = 4$s.

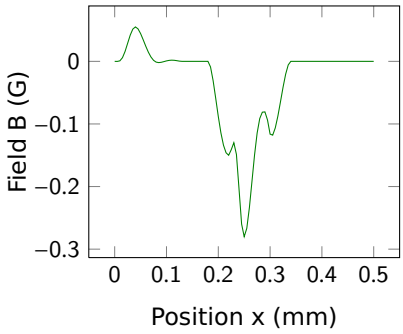

Figure 6.6. Magnetic field disturbances assumed for the simulation to match the measurements.

6.4.2. Simulation

For the simulation of the transport the measured magnetic field disturbances were modeled as a smooth function depicted in figure 6.6. The transport ramp $x_t(t)$ was constructed by interpolating the start point $(x_t(0) = 0, t = 0)$ and the end point $(x_t(t_t) = 0.5\,\mathrm{m}, t_t)$ with a vanishing first (velocity) and second (acceleration) derivative at both points. The trap frequency for the real transport geometry was determined using our BLASTIA TRAPSIMULATOR program. For lithium with $m = 6\,\mathrm{amu}$ and $\mu = \mu_B$ in the $|3\rangle$ state in a 70 G field (see [48]) the trap frequency is $\omega_B = 2\pi \cdot 6\,\mathrm{Hz}$. This gives a curvature in the trapping direction of the magnetic field

$$c_B = \frac{\omega_B^2 m}{\mu}$$

of $1.5\,\mathrm{G/cm^2}$.

With all this values plugged in the equation of motion (6.2) is integrated up to $t_\infty = 1.2\,t_t$. One can see in figure (6.7a) the trap frequency is the crucial parameter for the transport as the heating drastically increases for $\omega < 2\pi \cdot 5\,\mathrm{Hz}$, whereas a variation of the transport speed (by changing t_t) only does smaller changes. Both plots show resonant-like features. This is probably happens when the deceleration is "synchronized" with the oscillation frequency such that the kinetic energy caused by the heating is partially removed again.

For finite initial temperatures/velocities the plot does not change quantitatively. The heating is almost not affected at all. The plots 6.7a and 6.7b just get a small higher-frequency modulation. This would supposably lead to smearing out of the resonance feature for a realistic initial velocity distribution.

6.5. Discussion

Trap frequency The transport frequency of $\omega_B = 2\pi \cdot 6\,\mathrm{Hz}$ that could be achieved in our system is very low. Nevertheless the simulations showed that careful design and selection a materials could limit the heating to about $1\,\mu\mathrm{K}$. These results caused us to upgrade our gate valve to the highest grade of non-magnetic gate valves VAT has to offer.

Another problem arouses when one tries to transport a spin-mixture of lithium instead of a polarized gas in the $|3\rangle$ state. Spin-mixtures have the advantage that they evaporate themselves during the transport. Other groups recently managed to transport lithium mixtures in an ODT transport. In order to avoid loss due to hyperfine changing inelastic collisions a mixture of the lowest two states$|1\rangle + |2\rangle$ should be used[48], but then the effective magnetic

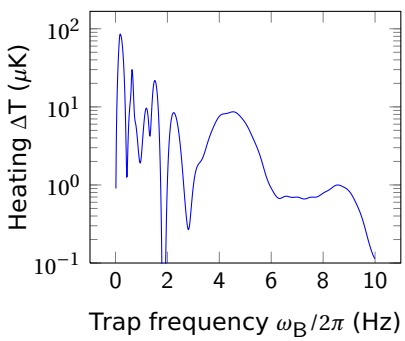

(a) Heating for various trap frequencies and a transport time $t_t = 4$s.

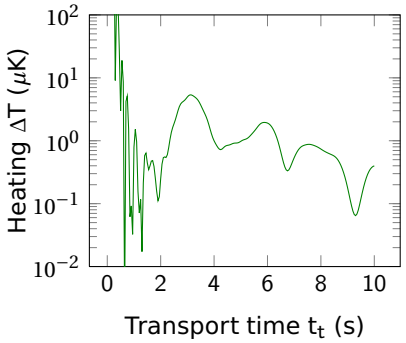

(b) Heating for transport speeds and a trap frequency of $\omega_B = 2\pi \cdot 6$Hz.

Figure 6.7. Heating under variation of different parameters.

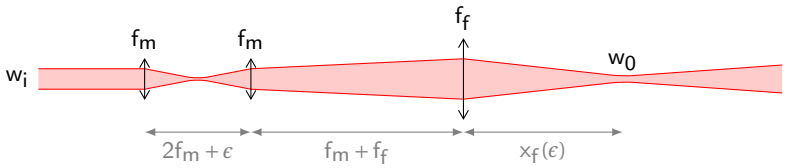

Figure 6.8. Proposed setup to move a focused beam over larger distances by moving one lens only very slightly with a piezo.

moment at 70 G and thus the trap frequency would even be lower.

Focusing A problem becomes apparent when one actually calculates the dipole force that is holding the atoms against gravity. It turns out that the radial intensity gradient of a Gaussian beam, where the Rayleigh range z_R is equal to the transport distance of 0.5 m and thus having a waist of $w_0 = \sqrt{z_R \lambda/\pi} \approx 400\,\mu$m is too weak to hold even the lithium atoms for reasonable (a few ten watts) laser powers. And for the same reason it is also not possible to transport the sodium ($m = 23$ amu) at all with an only weakly focused (100 μm) beam.

To solve that problem one has to shift the focus for a few Rayleigh ranges. This could be done by moving the focus of a tightly focused (nearly diffraction limited) beam by the same multiple of the now shorter Rayleigh range and magnifying the shift using a telescope.

The most promising solution is two short focal length microscope objectives f_m, where the first one is mounted on piezo stage that can move by $\epsilon = -\epsilon_{max}/2 \ldots \epsilon_{max}/2$ around the $2f$ position. The second microscope builds a $4f$ imaging system with another long focal length focusing lens f_f that projects the transport beam (figure (6.8)). Assuming a colli-

mated input beam with waist w_i, ray-transfer-matrix ($ABCD$ matrix) analysis gives a following intuitive formula for the distance of the focus after the last lens as a function of the displacement of the first objective ϵ:

$$x_\mathrm{f}(\epsilon) = x_0 - \left(\frac{f_\mathrm{f}}{f_\mathrm{m}}\right)^2 \epsilon,$$

where the central focus position

$$x_0 = f_\mathrm{f} \frac{\left(\pi w_\mathrm{i}^2\right)^2 + f_\mathrm{m}(f_\mathrm{m} - f_\mathrm{f})\lambda^2}{\left(\pi w_\mathrm{i}^2\right)^2 + f_\mathrm{m}^2\lambda^2}$$

is just $x_0 = f_\mathrm{f}$ in the limit of $\lambda \ll f_\mathrm{m,f}$. The waist at the focus w_0 is constant for small displacements ϵ:

$$w_0 = \frac{f_\mathrm{f}\lambda}{\pi w_\mathrm{i}} + \frac{f_\mathrm{f}\lambda}{f_\mathrm{m}\pi w_\mathrm{i}}\epsilon + \mathcal{O}\left(\epsilon^2\right).$$

Realistic values are $\lambda = 1064\,\mathrm{nm}$, $f_\mathrm{m} = 10\,\mathrm{mm}$, $f_\mathrm{f} = 300\,\mathrm{mm}$ and a piezo travel range of $\epsilon_\mathrm{max} = 400\,\mu\mathrm{m}$. The actual range of the focus shift can be preferably tuned by changing f_f and the focused waist by changing the initial beam size. But one should keep in mind that by increasing the magnification mechanical vibrations are magnified, too.

If one could find an optical fiber with the correct mode-diameter, the first objective could even be directly replaced with the fiber. Alternatively to the microscope objectives the focus could also be achieved by using a deformable mirror in a double-pass setup.

7. Outlook

With the recent achievement of the first trapped sodium atoms in the MOT our apparatus eventually made the step from only existing as a SOLIDWORKS CAD drawing to producing real cold atoms. Now the machine has to be extended so that we can proceed to get the Bose-Einstein condensate and later the degenerate Fermi gas. More electronics and software has to be developed to deal with the increasing complexity. When the transport is also mastered, we can start implement the actual experiment in our science chamber.

One big milestone on the way to the quantum simulator described in the introduction will be the Mott insulator with lithium, which has not been achieved by any group. In order to get the necessary lattice depth we plan to have a cavity-enhanced three-dimensional optical lattice, as realized in [16] for the one-dimensional case. By using a standing wave inside a cavity we also could benefit from the clean mode profile of the cavity. Disorder in a lattice is a limiting factor for many experiments.

A completely different direction of experiment would be the creation of hetero-nuclear NaLi molecules, which exhibit long-ranged dipolar interactions useful for quantum computation.

Whatever might come, we're well prepared - our flexible science chamber design lets us adapt to new questions and challenges that might come up in the fast evolving field of quantum simulation.

A. Technological Side Projects

A.1. Beam Steering

A.1.1. Overview

The daily realignment of our dear dye laser changes the beam pointing slightly every time. This misalignment is enough to significantly lower the fiber coupling efficiency into the multiple fibers. It is not enough to recouple a random fiber using a periscope that is placed directly after the laser beam exiting the dye laser. The optical setup with all its AOMs etc. is far too complex to conclude the beam alignment just by optimizing one single fiber coupling efficiency. For example it can happen that under a different angle the efficiency of an AOM is higher, thus compensating for a worse fiber coupling.

To overcome this limitation an independent and accurate measure of the beam pointing is required. The pointing of the laser beam has four degrees of freedom, two angular (pitch, yaw) and two spatial (horizontal and vertical offset). Ideally those could be (almost) independently measured in a setup given in figure A.1b. The position on the sensor 1 provides the offset. Due to the fact that a lens transforms angles into transverse position in the focus, sensor 2 measures the angle in respect to the "ideal" optical axis.

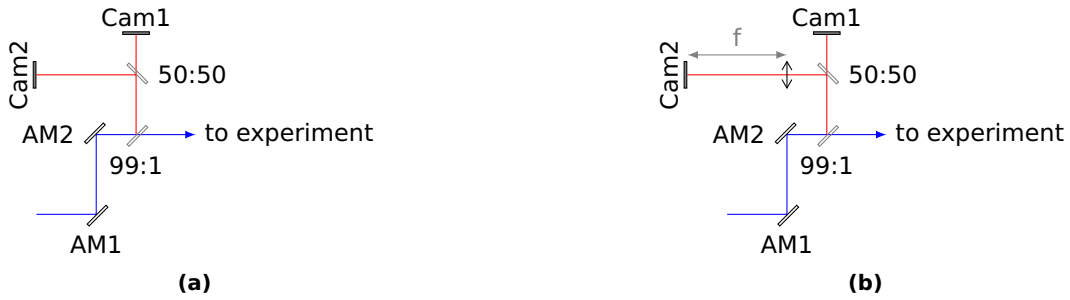

Figure A.1. Different implementations for the beam steering. AM1 and AM2 are two piezomotor actuated automated mirrors.

It has turned out that measuring the position of the beam on two sensors at different positions "downstream" is easier to implement (figure A.1a), sacrificing the decoupling of the mentioned four degrees of freedom. This is a minor drawback as the alignment will be performed by a computer program anyway. In addition if one uses cameras as sensors, one will also get information about the mode profile and collimation of the beam. On the contrary if the mode profile is deviating from a perfect Gaussian, the Fourier transformation of it that would be produced by the lens is not a Gaussian any more and thus harder to find a suited fit function.

A.1.2. Theory

This section will try to link the problem to control theory, especially to the state space formalism of linear control theory. But it should still be understandable without a background in this field.

The following method relies on the fact the system's response (angle and offset of the beam) is linear in the excitation or at least linearizeable around the operating point. This assumption applies to this problem very well, because the changes in the angle of the mirrors are very small, so that higher orders can be neglected.

The positions of the beam on both sensors (independent of which setup is used in detail) are combined into the *state vector*

$$\mathbf{x} = \begin{pmatrix} x_1 & y_1 & x_2 & y_2 \end{pmatrix}^{\mathrm{T}},$$

which equals the *output vector* ($\mathbf{y}$) in this particular case. The *input vector*

$$\mathbf{u} = \begin{pmatrix} h_1 & v_1 & h_2 & v_2 \end{pmatrix}^{\mathrm{T}}$$

describes the position of the horizontal and vertical mirror actuators. The response of the state vector to the input vector is ... in the *input matrix B*. For this specific problem the state vector is always in steady-state, because the position will only be updated after the mirrors are in their new position and have stopped moving. Thus the *state matrix A* is zero.

In general this development of such discrete-time time-invariant system is described by

following equations:

$$\mathbf{x}(k+1) = A\mathbf{x}(k) + B\mathbf{u}(k)$$
$$\mathbf{y}(k+1) = C\mathbf{x}(k)$$

The second equation is only for the sake of completeness, it has no deeper meaning for the beam steering problem, i.e. $C = \mathbb{1}$, feed forward D is completely omitted.

B has to be determined once using a separate step, the *system identification*. From the response $\mathbf{x}(k+i+1)$ to four orthogonal test excitations (e.g. move only one mirror axis at a time, $\mathbf{u}(k+i) = \begin{pmatrix} 0 & \dots & 1 & \dots & 0 \end{pmatrix}$) its elements can be calculated. Technically only the relative change $\delta\mathbf{u}$ can be used, because the absolute position of the mirror actuators is unknown unless a position sensor/encoder is used. Hence

$$B = \frac{\delta\mathbf{x}(k+1)}{\delta\mathbf{u}(k)}$$

looks like a Jacobian, but is strictly speaking only a difference quotient version of it.

Eventually one can calculate the required absolute mirror positions $\mathbf{u}(k)$ or relative movement $\delta\mathbf{u}(k)$ respectively to bring the laser beam to back the desired positions $\mathbf{x}(k+1)$ on the two sensors, to the set point.

$$\mathbf{u}(k) = B^{-1}\mathbf{x}(k+1)$$

The inverse input matrix B^{-1} has decoupled the degrees of freedom.

It turns out that it's not favorable to jump the set point directly, because even small model-mismatches (noise during the system identification, etc.) can cause instability. Worst case the positions oscillate around the setpoint and diverge. Thus one should approach the setpoint in several steps along a so called *reference trajectory*[1]. The simplest form is an exponential function: one tries to jump only a given percentage $0 < \lambda < 1$ towards the setpoint and consequently adds damping to the process. The optimum value for λ has to be found experimentally, but 0.75 should be a good starting point.

A.1.3. Experimental realization

Our system is designed to provide offline beam steering in contrary to active continuous beam stabilization. I.e. The mirrors keep their alignment once the beam is steered to the desired location and angle. Thus we chose to use mirror mounts that are motorized using

[1] Strictly speaking we only have a reference *point* as only a single step in the future is considered.

a piezo motor rather than a “pure” piezo. Active stabilization could more easily be implemented using piezo mirrors and four-quadrant photodiodes, stabilized using a controller of your choice (analog, digital).

Piezo motors exploit the difference between static and dynamic friction (slip stick effect) to move an actuator. By applying a sawtooth-like voltage on a piezo crystal it contracts/expands slowly in one direction sticking to the part that is supposed to be moved (static friction). The expansion/contraction motion is performed as fast as possible so that the piezo virtually doesn't move the part (dynamic friction).

In our experiment we are using two kinds of motorized mirror mounts. For automatized fiber coupling we are working with NEWPORT's AGILIS mirror mounts, which have a linear piezo motor simply moving the mirror directly. However for the beam steering of the high-power dye laser beam NEWFOCUS' 8807 motorized mirror mounts have proven more suited. The piezo motor is acting on a usual threaded mirror mount adjuster. This makes it more robust against accidentally bumping (I don't want to have a 2 W laser beam suddenly shooting randomly across the lab) and makes an additional pair of manual actuated mirrors for initial alignment obsolete.

The algorithm described in section A.1.2 is embedded into the BLASTIA framework, our experiment control software. The angle and position of the laser beam is determined by measuring its position on two CMOS cameras. In our case we're using two MIGHTEX BTE-B050-U CMOS cameras with 5 Mpx 1/2.5 in sensor. A small amount of laser beam is picked up at a single position in the beam, but travels different distances to each camera und thus decouples the angle and offset position.

A.1.4. Performance

With our setup we can reach sub-pixel resolution ($< 2.2\,\mu$m) and it usually takes about 5 steps from a slightly misaligned beam before the correct position is reached. The behavior of the system for a strongly misaligned beam is show in figure A.2. It can be seen that the vertical coordinate deviates from the expected curve due to some model-mismatch.

Because of the mode of operation of the piezo motors the actual change in position for a given number of steps/clicks is different in forward and backward direction. We found the ratio between the change in the angle in backward and forward direction with the same number of steps to be around 1.08.

We also experimented with using a lens instead of a longer optical path length to extract the angle information of the beam, but it neither saved us space nor was the decoupling

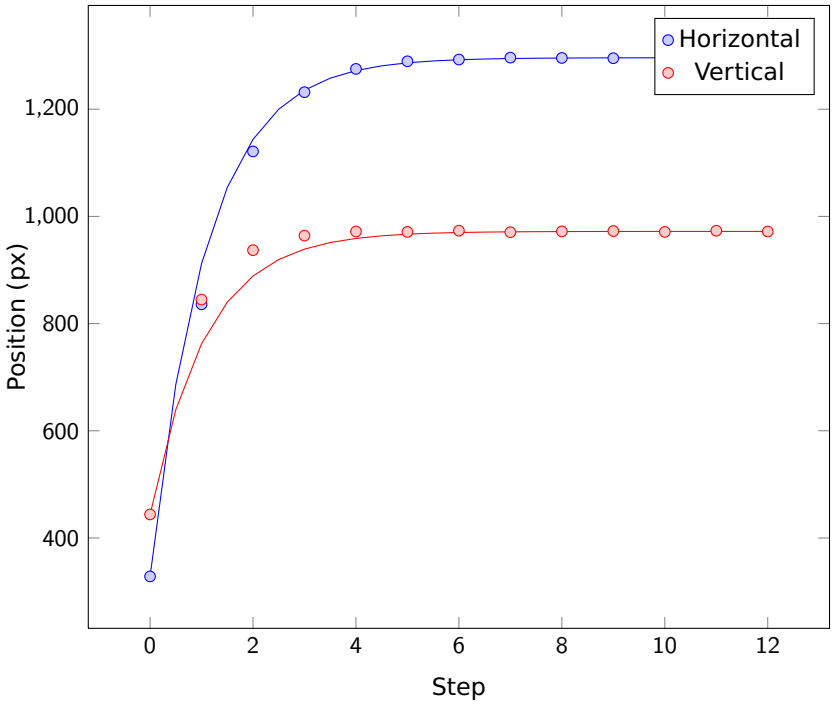

Figure A.2. Approaching the setpoints for a strongly misaligned beam. Ideally the measured points should be on the solid lines representing the exponential transient response with $\lambda = 0.75$.

significantly better. Actually to have the same angular resolution the focal length of the lens would have to be of the same distance as the path length of the just freely propagating laser beam.

A.1.5. Possible Improvements

The main limitation of our current system is that the determination of the beam center on the cameras by doing a 2D Gaussian fit (in a smaller range of interest) take about 10 s per camera. This slows down the whole beam steering process a lot. Smarter ways to find the position could be implemented, for example only using the location of the peak as parameter and keeping width, height and background offset constant or even just find the center of mass.

In order to account for non-linearities in the model one could also update the input matrix on the fly by also taking the most recent points into account instead of a fixed matrix that once was determined by the system identification. The singular value decomposition and the pseudo-inverse would be a useful tool for this.

A.2. Other projects

Despite the beam steering that was explained in detail, countless other smaller and bigger software and hardware projects have been developed in the course of this work. Just to mention a few, the projects ranged from a tiny usb-controlled three axis magnetic field, over a box controlling our pneumatic gate valves to a FPGA-driven multi-channel DDS frequency source working up to 400 MHz (and even higher in the super-nyquist mode).

Bibliography

[1] L. Bragg, J. F. Nye, A dynamical model of a crystal structure, Proceedings of the Royal Society of London. Series A, Mathematical and Physical Sciences 190 (1023) (1947) 474–481. 7

[2] W. S. Bakr, J. I. Gillen, A. Peng, S. Folling, M. Greiner, A quantum gas microscope for detecting single atoms in a hubbard-regime optical lattice, Nature 462 (7269) (2009) 74–77. 7, 8

[3] J. Bardeen, L. N. Cooper, J. R. Schrieffer, Theory of superconductivity, Phys. Rev. 108 (5) (1957) 1175–1204. 8

[4] P. W. Anderson, Superconductivity in high-t_c cuprates: The cause is no longer a mystery, Physica Scripta T102 (2002) 10–12. 8

[5] R. E. Feynman, Simulating physics with computers, International Journal of Theoretical Physics 21 (6) (1982) 467–488. 8

[6] I. Bloch, J. Dalibard, W. Zwerger, Many-body physics with ultracold gases, Rev. Mod. Phys. 80 (3) (2008) 885. 8

[7] W. Hofstetter, J. I. Cirac, P. Zoller, E. Demler, M. D. Lukin, High-temperature superfluidity of fermionic atoms in optical lattices, Phys. Rev. Lett. 89 (22) (2002) 220407. 8

[8] J. Hubbard, Electron correlations in narrow energy bands, Proceedings of the Royal Society of London. Series A. Mathematical and Physical Sciences 276 (1365) (1963) 238–257. 8

[9] M. Greiner, O. Mandel, T. Esslinger, T. W. Hansch, I. Bloch, Quantum phase transition from a superfluid to a mott insulator in a gas of ultracold atoms, Nature 415 (6867) (2002) 39–44. 9

[10] R. Jordens, N. Strohmaier, K. Gunter, H. Moritz, T. Esslinger, A mott insulator of fermionic atoms in an optical lattice, Nature 455 (7210) (2008) 204–207. 9

[11] U. Schneider, L. Hackermuller, S. Will, T. Best, I. Bloch, T. A. Costi, R. W. Helmes, D. Rasch, A. Rosch, Metallic and insulating phases of repulsively interacting fermions in a 3d optical lattice, Science 322 (5907) (2008) 1520–1525. 9

[12] T. Köhler, K. Góral, P. S. Julienne, Production of cold molecules via magnetically tunable feshbach resonances, Rev.f Mod. Phys. 78 (4) (2006) 1311. 9

[13] A. M. Rey, R. Sensarma, S. Folling, M. Greiner, E. Demler, M. D. Lukin, Controlled preparation and detection of d-wave superfluidity in two-dimensional optical superlattices, EPL (Europhysics Letters) 87 (6) (2009) 60001 (6pp). 10

[14] S. Folling, S. Trotzky, P. Cheinet, M. Feld, R. Saers, A. Widera, T. Muller, I. Bloch, Direct observation of second-order atom tunnelling, Nature 448 (7157) (2007) 1029–1032. 10

[15] C. H. Schunck, M. W. Zwierlein, C. A. Stan, S. M. F. Raupach, W. Ketterle, A. Simoni, E. Tiesinga, C. J. Williams, P. S. Julienne, Feshbach resonances in fermionic ^{6}Li, Phys. Rev. A: At., Mol., Opt. Phys. 71 (4) (2005) 045601. 11

[16] A. Mosk, S. Jochim, H. Moritz, T. Elsässer, M. Weidemüller, R. Grimm, Resonator-enhanced optical dipole trap for fermionic lithium atoms, Opt. Lett. 26 (23) (2001) 1837–1839. 11, 64

[17] H. Metcalf, P. V. der Straten, Laser cooling and trapping, Springer, 1999. 12

[18] C. Pethick, H. Smith, Bose-Einstein condensation in dilute gases, Cambridge University Press, 2002. 18

[19] C. Stan, W. Ketterle, Multiple species atom source for laser-cooling experiments, Rev. Sci. Instrum. 76 (2005) 063113. 19, 26

[20] J. O'Hanlon, A user's guide to vacuum technology, Wiley, 2003. 20

[21] R. R. Addis, L. Pensak, N. J. Scott, Evaluation of a new fluoroelastomer as a gasketing material for high vacuum systems, in: Transactions of the Seventh National Symposium on Vacuum Technology, Pergamon Press, Ltd., 1960, pp. 39–44. 21

[22] D. J. Crawley, L. de Csernatony, Degassing characteristics of some o ring materials, Vacuum 14 (7) (1964) 7–9. 21

[23] D. S. Naik, Bose-einstein condensation: Building the testbeds to study superfluidity, Ph.D. thesis, Georgia Institute of Technology (Dec 2006). 27

[24] J. V. Prodan, W. D. Phillips, H. Metcalf, Laser production of a very slow monoenergetic atomic beam, Phys. Rev. Lett. 49 (16) (1982) 1149–1153. 28

[25] T. Schuster, A novel apparatus for experiments with ultracold sodium and lithium, Diploma thesis, Kirchhoff Institute for Physics (2008). 33, 42, 49

[26] C. A. Stan, Experiments with interacting bose and fermi gases, Ph.D. thesis, Massachusetts Institute of Technology (Jul 2005). 36, 53

[27] E. Mimoun, L. D. Sarlo, J.-J. Zondy, J. Dalibard, F. Gerbier, Sum-frequency generation of 589 nmlight with near-unit efficiency, Opt. Express 16 (23) (2008) 18684–18691. 40

[28] D. A. Steck, Sodium D line data, `http://steck.us/alkalidata` (revision 2.1.3) (Aug 2009). 41

[29] R. W. P. Drever, J. L. Hall, F. V. Kowalski, J. Hough, G. M. Ford, A. J. Munley, H. Ward, Laser phase and frequency stabilization using an optical resonator, Appl. Phys. B: Lasers Opt. 31 (2) (1983) 97–105. 42

[30] G. C. Bjorklund, Frequency-modulation spectroscopy: a new method for measuring weak absorptions and dispersions, Opt. Lett. 5 (1) (1980) 15–17. 42

[31] E. L. Raab, M. Prentiss, A. Cable, S. Chu, D. E. Pritchard, Trapping of neutral sodium atoms with radiation pressure, Phys. Rev. Lett. 59 (23) (1987) 2631–2634. 43, 46

[32] J. Weiner, V. S. Bagnato, S. Zilio, P. S. Julienne, Experiments and theory in cold and ultracold collisions, Rev. Mod. Phys. 71 (1) (1999) 1–85. 46, 47

[33] A. Gallagher, D. E. Pritchard, Exoergic collisions of cold Na^*-Na, Phys. Rev. Lett. 63 (9) (1989) 957–960. 47

[34] M. Prentiss, A. Cable, J. E. Bjorkholm, S. Chu, E. L. Raab, D. E. Pritchard, Atomic-density-dependent losses in an optical trap, Opt. Lett. 13 (6) (1988) 452–454. 47

[35] T. Walker, D. Sesko, C. Wieman, Collective behavior of optically trapped neutral atoms, Phys. Rev. Lett. 64 (4) (1990) 408–411. 47

[36] D. W. Sesko, T. G. Walker, C. E. Wieman, Behavior of neutral atoms in a spontaneous force trap, J. Opt. Soc. Am. B 8 (5) (1991) 946–958. 47

[37] W. Ketterle, K. B. Davis, M. A. Joffe, A. Martin, D. E. Pritchard, High densities of cold atoms in a dark spontaneous-force optical trap, Phys. Rev. Lett. 70 (15) (1993) 2253–2256. 47, 48

[38] M. H. Anderson, W. Petrich, J. R. Ensher, E. A. Cornell, Reduction of light-assisted collisional loss rate from a low-pressure vapor-cell trap, Phys. Rev. A 50 (5) (1994) R3597–R3600. 48

[39] J. Goldwin, S. B. Papp, B. DeMarco, D. S. Jin, Two-species magneto-optical trap with ^{40}K and ^{87}Rb, Phys. Rev. A 65 (2) (2002) 021402. 49

[40] Z. Hadzibabic, C. A. Stan, K. Dieckmann, S. Gupta, M. W. Zwierlein, A. Görlitz, W. Ketterle, Two-species mixture of quantum degenerate bose and fermi gases, Phys. Rev. Lett. 88 (16) (2002) 160401. 49

[41] Z. Hadzibabic, S. Gupta, C. A. Stan, C. H. Schunck, M. W. Zwierlein, K. Dieckmann, W. Ketterle, Fiftyfold improvement in the number of quantum degenerate fermionic atoms, Phys. Rev. Lett. 91 (16) (2003) 160401. 51

[42] K. B. Davis, M. O. Mewes, M. R. Andrews, N. J. van Druten, D. S. Durfee, D. M. Kurn, W. Ketterle, Bose-einstein condensation in a gas of sodium atoms, Phys. Rev. Lett. 75 (22) (1995) 3969–3973. 52

[43] D. S. Naik, C. Raman, Optically plugged quadrupole trap for bose-einstein condensates, Phys. Rev. A 71 (3) (2005) 033617. 52

[44] H. Lewandowski, D. Harber, D. Whitaker, E. Cornell, Simplified system for creating a bose-einstein condensate, J. Low Temp. Phys. 132 (5) (2003) 309–367. 54

[45] M. Greiner, I. Bloch, T. W. Hänsch, T. Esslinger, Magnetic transport of trapped cold atoms over a large distance, Phys. Rev. A 63 (3) (2001) 031401. 54

[46] S. Schmid, G. Thalhammer, K. Winkler, F. Lang, J. H. Denschlag, Long distance transport of ultracold atoms using a 1d optical lattice, NJP 8 (8) (2006) 159. 55

[47] T. L. Gustavson, A. P. Chikkatur, A. E. Leanhardt, A. Görlitz, S. Gupta, D. E. Pritchard, W. Ketterle, Transport of bose-einstein condensates with optical tweezers, Phys. Rev. Lett. 88 (2) (2001) 020401. 55

[48] M. E. Gehm, Properties of ^{6}Li, available from: http://www.phy.duke.edu/research/photon/qoptics/techdocs/ (Feb 2003). 61